Cell Reports

Article

Catalytic footprints of DNMT1 dynamics during mammalian cell state transitions

Graphical abstract

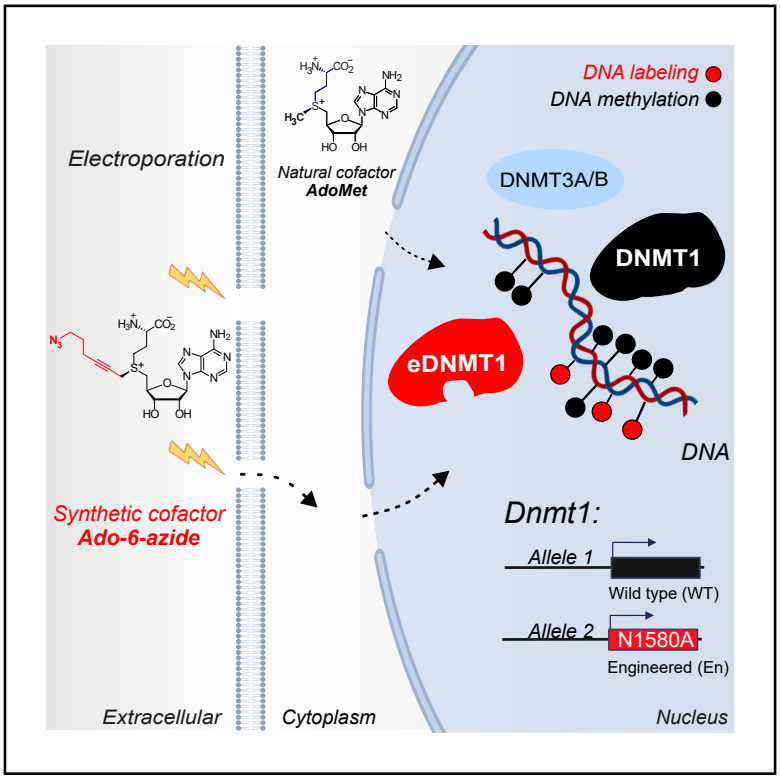

Highlights

- An ESC line with chromosomally expressed wild-type and sterically engineered DNMT1
- Chemical mapping of DNMT1 catalysis during naive-to-primed transition in live mESC
- DNMT1 contributes to *de novo* methylation of germline-associated genes
- DNMT1 methylation competes with active demethylation at boundaries of CpG islands

Authors

Vaidotas Stankevičius, Kotryna Kvederavičiūtė, Liepa Gasiulė, Audronė Rukšėnaitė, Giedrius Vilkaitis, Saulius Klimašauskas

Correspondence

giedrius.vilkaitis@bti.vu.lt (G.V.), saulius.klimasauskas@bti.vu.lt (S.K.)

In brief

Stankevičius et al. report mono-allelic engineering of mESCs enabling DNMT1 catalysis-dependent tagging of genuine target sites upon internalization of a synthetic cofactor analog. Genomic mapping of DNMT1 catalysis during naïve-to-primed transition unveiled profound DNMT1 methylation of germline genes and sites of active demethylation at boundaries of CpG islands.

Stankevičius et al., 2026, Cell Reports *45*, 117435
June 23, 2026 © 2026 The Author(s). Published by Elsevier Inc.
https://doi.org/10.1016/j.celrep.2026.117435

CellPress

Cell Reports

CellPress
OPEN ACCESS

Article

Catalytic footprints of DNMT1 dynamics during mammalian cell state transitions

Vaidotas Stankevičius,[1,2] Kotryna Kvederavičiūtė,[1,2] Liepa Gasiulė,[1] Audronė Rukšėnaitė,[1] Giedrius Vilkaitis,[1,*] and Saulius Klimašauskas[1,3,*]

[1]Institute of Biotechnology, Life Sciences Center, Vilnius University, 10257 Vilnius, Lithuania
[2]These authors contributed equally
[3]Lead contact
*Correspondence: giedrius.vilkaitis@bti.vu.lt (G.V.), saulius.klimasauskas@bti.vu.lt (S.K.)
https://doi.org/10.1016/j.celrep.2026.117435

SUMMARY

5-methylcytosine is a reversible regulatory mark in mammalian genomes whose distribution varies across genetic loci, cell types, and disease conditions. Cytosine-5 methylation is brought about by three AdoMet-dependent DNA methyltransferases (DNMTs) with primary tasks in *de novo* (DNMT3A and DNMT3B) or maintenance (DNMT1) methylation. However, the precise roles and interplay between the three methylation "writers" remain obscure. To selectively track an individual DNMT, we derived a heterozygous mESC line with chromosomal alleles expressing the wild-type and a sterically engineered variant of DNMT1. This enables catalysis-dependent chemical tagging DNMT1 methylation sites upon in-cell delivery of a synthetic AdoMet analog. Genome-wide mapping of the DNMT1 catalysome during naive-to-primed transition of mESC shows that DNMT1 contributes to *de novo* methylation of germline genes and competes with active demethylation at boundaries of CpG islands. Altogether, we provide a unique tool for chemical monitoring of individual methylation writers in minimally perturbed developmental and disease models.

INTRODUCTION

Epigenetic regulation of cell identity via reversible changes in DNA modification and chromatin structure plays a central role in mammalian development. The key DNA modification mechanism is methylation of cytosine to 5-methylcytosine (m^5C) in the context of CpG dinucleotides, whose genomic distribution varies across different genetic loci, cells, and tissues. The DNA methylation in mammalian cells is brought about by three "writers"—catalytically active DNA methyltransferases (DNMTs), DNMT1, DNMT3A, and DNMT3B,[1,2] which use the *S*-adenosyl-L-methionine (AdoMet) cofactor as the methyl group donor. On the reverse pathway, DNA methylation can be "erased" via enzymatic oxidation of m^5C by the three TET oxygenases (TET1, TET2, and TET3) to yield 5-hydroxymethylcytosine,[3–5] 5-formylcytosine, or 5-carboxylcytosine.[6] Alternatively, DNA methylation can be lost in a replication-dependent manner in the absence of maintenance methylation (passive demethylation).

Deletions of these enzymes invoke embryonic (*Dnmt1* and *3b*) or postnatal (*Dnmt3a*) mortality in mice, indicating their critical role in executing mammalian developmental programs, whereas perturbed regulation affecting DNA modifying enzyme activity has been linked to a variety of disorders ranging from facial abnormalities (ICF) syndrome to cancer.[7] Therefore, DNA methylation profiling remains imperative to uncover the regulatory mechanisms associated with both developmental and disease-associated contexts.

Although DNA methylation is essential for mammalian development, the precise roles and interplay among the three epigenetic writers remain far from understood.[8] DNMT1 was shown to perform processive methylation of hemimethylated CpG sites[9,10] and was assigned a primary role in maintaining the established methylation patterns through cycles of DNA replication. In contrast, DNMT3A and DNMT3B have no such substrate preference and are thought to be largely responsible for establishing *de novo* methylated regions in the genome. However, increasing numbers of studies have indicated significant redundancy and compensatory activity among the three methylation "writers."[11–15] Yet, the attribution of the methylation marks deposited by a particular DNMT is impeded by several methodological limitations.[16,17] This is primary because analysis of genomic DNA using the well-established m^5C profiling techniques yields an aggregate DNA methylation signal arising from the collective action of the three DNMTs and three TETs, which obscures information on individual enzymatic contributions. Attempts to address this issue through *Dnmt* knockouts (KOs),[18] CRISPR scanning,[19] or degron[20] approaches typically induce massive undermethylation of the genome and associated phenotypic alterations, which hinders the determination of the DNMT-specific activities in live cells. On the other hand, elevated levels of DNMT1 may lead to aberrant gene imprinting triggering embryonic lethality,[21] whereas overexpression of DNMT1 in mouse embryonic stem cells (mESCs) results in DNA methylation patterns that closely resemble cancer methylomes, marked by global

This is an open access article under the CC BY-NC-ND license (http://creativecommons.org/licenses/by-nc-nd/4.0/).

hypomethylation and focal hypermethylation in promoters and CpG islands (CGIs).[22] While restoring DNMT1 activity can mitigate the consequences of its deficiency, only partial recovery is attainable,[23] obstructing the determination of the MTase-specific activities under physiologically relevant conditions. The roles of individual DNMTs can indirectly be inferred from the level of gene expression and/or genomic localization of the proteins. However, spatial association alone may not be a good proxy for DNA methylation as the catalytic activity of DNMTs is strongly regulated by post-translational modifications[24–26] and interactions with external factors.[1,6,27]

mESCs is a model of choice for epigenetic studies as they can be maintained *in vitro* to resemble two reversible forms of an early preimplantation stage. Cells grown with two small-molecule inhibitors (2i); MEKi and GSKi closely mimic inner cell mass and are regarded as the ground or naive state of pluripotency.[28] The inhibitors suppress DNMTs via transcriptional repression and protein degradation, resulting in hypomodification of the genome[29]; mESCs cultivated in serum and leukemia inhibitory factor (LIF)-enriched conditions resemble early epiblast cells and are characterized by a hypermethylated "primed" state exhibiting expression of many lineage-specific genes.[30,31]

In an initial attempt to address the challenges mentioned previously, we have generated an mESC line that expressed a sterically engineered (N1580A) variant of DNMT1 permitting selective chemical tagging of the DNMT1 methylation sites upon pulse-internalization of an extended synthetic analog of the AdoMet cofactor, Ado-6-azide.[32] However, these cells contained a bi-allelic replacement of genomic *Dnmt1* and thus showed a significantly reduced DNA methylation levels due to weaker acceptance of the natural AdoMet cofactor by the engineered DNMT1 variant. In this work, we successfully overcome this drawback by resorting to next-generation genome editing tools[33] to derive an mESC line with a mono-allelic *Dnmt1* N1580A substitution, which ensured endogenously regulated expression of both the wild-type (WT) and the engineered *Dnmt1* variants within the same cell (Figure 1A). Through whole genome bisulfite sequencing (WGBS), we demonstrate that these cells exhibit a genome-wide CpG methylation distribution strikingly similar to that of the parental line. The readout of DNMT1-specific epigenetic landscapes exhibited good concordance with WGBS and reduced representation bisulfite sequencing (RRBS) profiles, validating general applicability of the developed platform for epigenome research. In particular, it enabled facile detection of regions undergoing active methylation/demethylation at CGI boundaries and actively transcribed genes. Finally, the engineered cells were further validated in a detailed study of the DNMT1-specific events that occur during the naïve-to-primed transition in live mESCs. Our study reveals that, besides its canonical maintenance activity, DNMT1 contributes to *de novo* methylation of promoter CGIs associated with germ cell genes. Taken together, our study demonstrates a unique tool suitable for temporal monitoring of individual DNA methylation writers in live mammalian cells representing early mouse embryogenesis or disease-specific biological settings.

RESULTS

Establishment and characterization of mono-allelic *Dnmt1* N1580A cells

Previously, we have described CRISPR-Cas9-directed production of a homozygous mouse embryonic stem cell line containing both engineered *Dnmt1* N1580A alleles. Since no clones with a mono-allelic *Dnmt1* substitution were obtained using this approach, we employed editing which avoids double-strand breaks or template-guided homologous DNA end-joining[33] (Figure S1A). The desired construct was obtained with 15% efficiency (Figure 1B) judging from restriction endonuclease mapping of 121 clones. Sanger sequencing of three selected mono-allelic clones confirmed error-free engineering of their *Dnmt1* locus (Figure S1B).

Next, we went on to compare the behavior of the produced mono-allelic cell line with the bi-allelic engineered *Dnmt1* variant, WT and bi-allelic KO mESC lines (referred to as WT/En, En/En, WT, and KO cells, respectively). Cells were cultivated in the presence of serum and LIF with or without the 2i kinase inhibitors, which are known to confer distinct embryonic cell states linked with characteristic global DNA methylation patterns[34] (Figure 1C). To exclude potential artifacts arising from genome editing, we verified the gene expression and cellular protein levels of the three DNMTs and a tightly associated regulator protein, UHRF1, to well match those of the WT cells in both cultivating conditions (Figures 1D and 1E; Figure S2). In line with previous observations,[31,35,36] the abundance of all four proteins was significantly suppressed in all cells exposed to the 2i inhibitors.

Given the uniformity of the *Dnmt* expression profiles of the four cell lines concerned, we analyzed their global m^5C levels using high-performance liquid chromatography tandem mass specrometry (HPLC-MS/MS) (Figure 1F). We found the DNA methylation in the mono-allelic WT/En cells to be substantially higher than in the homozygous En/En cells and nearly identical to that of the WT cells under LIF conditions. At a single gene level, Sanger bisulfite sequencing (Sanger BS-seq) methylation patterns in selected *Sfi1, H1fnt*, and *Fryl* CGI regions also exhibited a substantial similarity between WT and heterozygous WT/En cells (Figure S3).

Next, we went on to further compare the cell lines (Figure 2A) at the base resolution methylome level. Akin to HPLC-MS/MS measurements, WGBS analysis showed a remarkably similar distribution of the global DNA methylation levels in the WT/En and WT cells with roughly 70% CpG methylation coverage (Figures 2B and 2C); the engineered WT/En cells retained methylation profiles across a range of genomic features, including coding genes and pseudogenes, repetitive elements and *cis*-regulatory elements (Figures 2D–2F; Figures S4A and S4B). Moreover, a detailed genome-wide analysis of CpG island m^5C showed concordant methylation profiles along intragenic, intergenic and promoter CGIs (Figure 2G; Figure S4C) as well as at the individual CGI level, including CGI regions of the *Sfi1*, *H1fnt*, and *Fryl* gene promoters, which were previously identified as the most prevalent meiosis and development-related DNMT1-specific modification loci in the biallelic En/En cells[32] (Figure 2H; Figures S3 and S4D), with a slightly reduced fraction of the top methylated targets over all chromosomes (Figure S5).

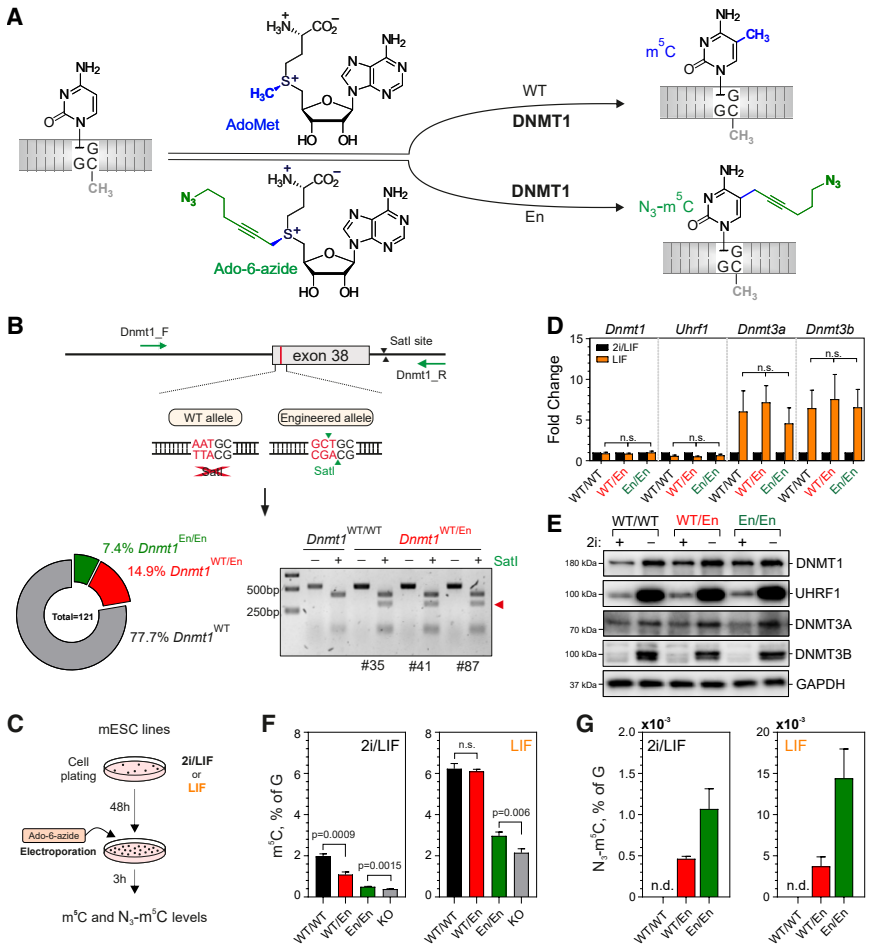

Figure 1. Design and characterization of *Dnmt1* allele-engineered mouse embryonic stem cells

(A) Modification of hemimethylated CpG sites in DNA catalyzed by the wild-type (WT) and engineered (En) variants of DNMT1.

(B) Engineering of monoallelic *Dnmt1* N1580A mouse embryonic stem cells using search-and-replace genome editing. SatI restriction analysis of a PCR-amplified locus in selected clones (out of 121 analyzed) confirms a heterozygous AAT→GCT substitution, which gives a 312 bp fragment (indicated by an arrow) originating from a new Sat site in the engineered allele along with a 419 bp fragment originating from the WT allele.

(C) Experimental workflow for analysis of gene and protein expression, global DNA methylation levels, and DNMT1-directed tagging of endogenous DNA targets in WT, *Dnmt1*$^{WT/N1580A}$ (WT/En), *Dnmt1*$^{N1580A/N1580A}$ (En/En), and *Dnmt1* KO mESC lines electroporated with synthetic cofactor Ado-6-azide. Cells were cultured for 48 h in 2i/LIF or LIF.

(D) Quantitative RT-PCR analysis of selected methyltransferase mRNA levels in WT and engineered mESC lines cultured in LIF or 2i/LIF medium. Bars represent fold change mean ± SD, n = 4 independent experiments; n.s., not significant.

(E) Western blot analysis of DNMT and UHRF1 protein levels in mESC lines cultured in LIF medium with or without 2i.

(F) HPLC-MS/MS analysis of genomic m^{5}C levels in mESCs evaluated as (%) of dG. Bars denote mean ± SD, n = 3 independent experiments.

(G) HPLC-MS/MS analysis of genomic N_3-m^{5}C levels in the mESC lines after the electroporation with 500 μM Ado-6-azide. Bars denote mean ± SD, n = 3 independent experiments; n.d., not detected.

The bi-allelic En/En cells showed significantly reduced DNA methylation similar to that of the KO cells under LIF conditions.

Genome-wide DNA tagging in mono-allelic *Dnmt1* N1580A cells

In the next step, we performed a comparative analysis of the deposited bio-orthogonal azide marks in the engineered mESC lines cultivated in LIF medium after electroporation with 1 mM Ado-6-azide (Figure 3A). Pleasingly, HPLC-MS/MS analysis of genomic DNA showed considerable intragenomic incorporation of N_3-m^{5}C in the WT/En cells in a cell state- and dose-dependent manner (Figures 1G; Figures S6A and S6B). The observed levels were approximately 2- to 3-fold lower than those in the bi-allelic En/En cells consistent with a 2-fold depletion of the engineered DNMT1 in the WT/En cells. This also illustrates the capacity of the mutant to compete for a proper share of the target sites in the presence of the WT enzyme and thus pointing at a fairly even genomic distribution of the two MTase types.

To look at the genome-wide distributions of the azide tags, the DNA was subjected to profiling using the Tethered oligonucleotide-primed sequencing (TOP-seq) approach in which the azide groups were exploited for generating mappable amplicons

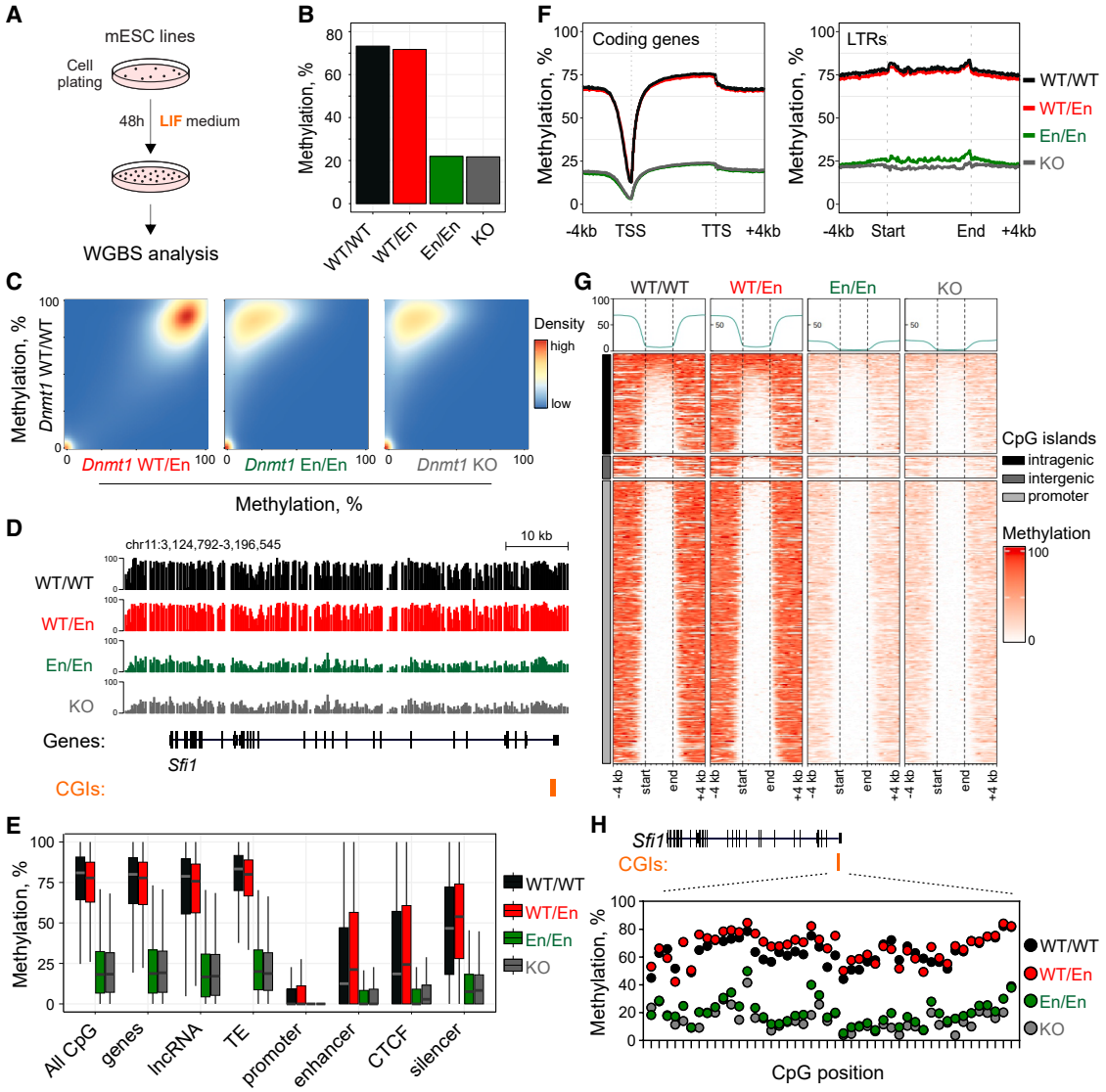

Figure 2. Engineered monoallelic *Dnmt1* N1580A mESCs sustain genome-wide DNA methylation maintenance

(A) Experimental workflow for WGBS analysis of mESC lines cultured in LIF medium.

(B) Global CpG methylation levels determined by WGBS.

(C) Density scatterplots comparing WT CpG methylation levels with WT/En, En/En, and KO mESC lines.

(D) Representative genome browser views of WGBS-derived DNA methylation patterns in mESCs lines. Each track denotes methylation of individual CpGs from 0% to 100%. Genes and CpG islands (CGI) are displayed beneath tracks.

(E) Boxplots of CpG methylation levels in different genomic features. Lines indicate median, box is limited by the upper and lower quartiles, and whiskers extend to 1.5*IQR.

(F) Distribution of CpG methylation along coding genes and long terminal repeats (LTRs), including 4 kb flanking sequences.

(G) WGBS heatmap representing CpG methylation levels in intragenic (black), intergenic (dark gray), and promoter (gray)-associated CpG islands in mESCs DNA methylation increases from unmethylated (white) to fully methylated (red) CpGs.

(H) CGI methylation in *Sfi1* gene determined with WGBS. Dots denote mean methylation level of individual CpGs. The WGBS and RRBS data were obtained from three independent cell clones that were pooled before analysis.

originating from adjoining genomic sequences.[37] The number of sequencing reads in triplicate Dnmt1-TOP-seq libraries acquired from ~1 M of engineered cells (about 120 M per biological replicate) was ~3 orders of magnitude higher than in the WT controls (Table S5). As a key quality measure, we checked the read start positions in the generated whole-genome sequencing libraries. Notably, we found that the majority (~90%) of mapped *Dnmt1* WT/En reads originated within 2 nt of a genomic CpG site (Figure 3B)—similar to those obtained in the bi-allelic En/En cells, and in stark contrast to the WT controls. Nor could we observe DNA modifications in CHH motifs (Figure S7A), clearly indicating that the genomic tagging in both engineered cell lines was

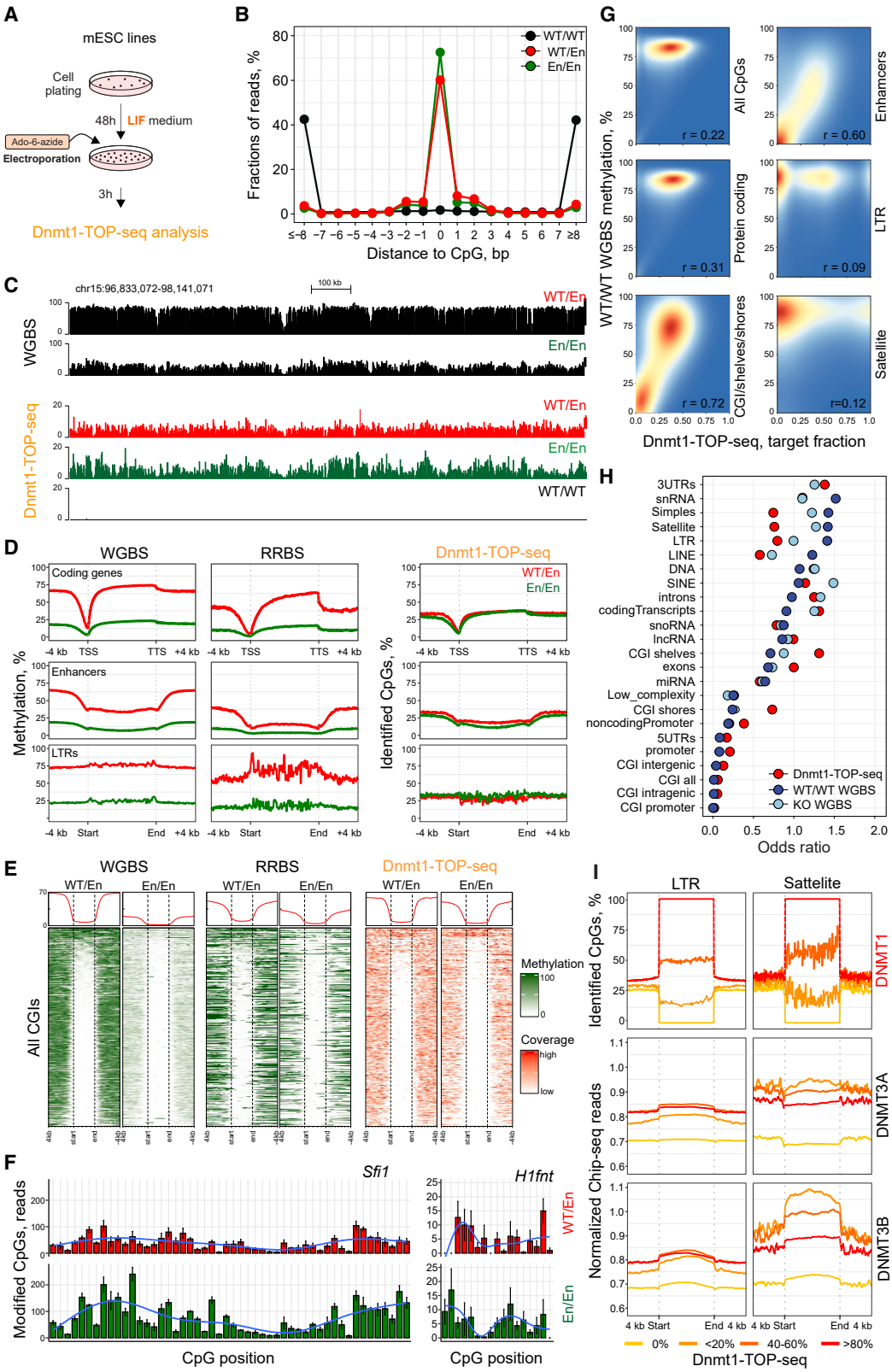

(legend on next page)

consistent with the known sequence specificity of DNMT1. The mean coverage of detected CpGs was approximately 10× per replicate encompassing 30% of genomic CpGs (Figures S7B and S7C), with even distribution across the chromosomes (Figure S7D). Correlation between biological replicates genome-wide and within individual genomic elements was slightly higher in the En/En than in the WT/En cells, consistent with their higher level of chemical tagging (Figures S7E–S7G).

We next compared the genome-wide distribution of identified CpG sites in the Dnmt1-TOP-seq libraries with the methylation levels determined by WGBS and RRBS. Genome browser views illustrated quite similar modification distribution in both engineered cells (Figure 3C) despite a clear disparity in their global m^5C levels. Moreover, both engineered cell lines showed remarkably similar CpG tagging profiles across a variety of genomic elements (Figures 3D and 3E). Slight differences can be observed in *cis*-regulatory regions, including enhancers, and DNA repeat elements, including long terminal repeats (LTRs) (Figure 3D; Figure S8) as well as at the single CGI level (Figure 3F). Altogether, the mono-allelic WT/En cells showed a sufficiently robust Dnmt1-TOP-seq signal in the context of a highly realistic DNA methylation profile (as opposed to En/En), and thus proved superior for functional studies.

To further validate their utility, we compared WT/En Dnmt1-TOP-seq profile with DNA methylation (WGBS) profiles derived from the WT (Figure 3G; Figure S9) and WT/En cells (Figure S9) across a range of genetic elements and features. In the scatterplots, the Dnmt1-TOP-seq is displayed as target fraction (a fraction of identified targets within a 2 kb bin or element) versus mean CpG methylation within the same element for WGBS. Generally, the plots showed a rather good agreement between the two signals in genomic elements known to contain hypomethylated regions (enhancers, CGI border regions), whereas in highly methylated regions (protein coding and repeat elements), the WGBS signal (from WT or WT/En) was unmatched by the comparatively low Dnmt1-TOP-seq counts. Overall, we found that such straightforward comparison of the two signals was not particularly informative as distinct sampling techniques and different data scaling were used grossly obscuring biologically relevant signals.

To eliminate the influence of data mismatch and rectify signals reflecting biological processes, we performed functional enrichment analysis of the Dnmt1-TOP-seq data along with the WGBS signal in WT or KO cells across a range of genomic elements (Figure 3H). A notable enrichment in the Dnmt1 modification profile as compared to the WT WGBS signal was found at CGI shelves and shores as well as coding regions (exons, introns, and coding transcripts). Taking into account that the deposited azide tags are poor substrates for TET enzymes,[38] such enhanced DNMT1-TOP-seq signal (representing the DNMT1 methylation rate) may arise in regions that undergo rapid methylation/TET-dependent demethylation turnovers leading to low steady-state levels of m5C.[39,40] Indeed, previous studies found extensive TET-promoted demethylation of gene promoters and transcription start sites (TET1), or gene bodies and exon boundaries (TET2) in highly expressed genes.[41,42] On the other hand, certain repeat elements (satellites, simple, LINE, and LTRs) were much less enriched in Dnmt1-TOP-seq as compared to m^5C levels in WT cells. Notably, the KO cells also showed a weaker enrichment relative to WT control but the change magnitude was significantly larger in the Dnmt1-TOP-seq profile. These regions may undergo lower DNMT1 maintenance activity as compared to the rest of the genome.

To further disentangle the role of DNMTs in the formation and maintenance of DNA methylation in mESCs, we compared the DNMT1-specific modification with localization of DNMT3A and DNMT3B mapped by chromatin immunoprecipitation sequencing (ChIP-seq).[43] A fairly good correlation was found within intergenic, intragenic CGI, and enhancer elements in line with faithful maintenance of *de novo* methylation by DNMT1 (Figure S10A). On the other hand, the DNMT1 activity profiles showed poor correlation with the *de novo* methyltransferase binding at repetitive elements, including LTRs, SINEs, and LINEs (Figure 3I; Figure S10B), consistent with previous findings.[12] Remarkably, an even more complex DNMT interactome was observed in satellite and microsatellite regions showing an inverse association between the DNMT1 activity and the presence of DNMT3B (Figure 3I; Figure S10B).

We also looked at gene pathways that were associated with DNMT1-modified promoter CGIs. Gene Ontology (GO) analysis

Figure 3. Genomic distribution of DNMT1-specific azide tags in engineered *Dnmt1* N1580A cells

(A) Experimental workflow to profile genome-wide DNMT1-specific cytosine modifications in engineered and control mESCs. Cells were cultured for 48 h in LIF medium and electroporated with 1 mM Ado-6-azide.

(B) Distance distribution of read start positions to a nearest CpG site in the Dnmt1-TOP-seq libraries prepared from engineered (WT/En and En/En) and WT mESCs.

(C) Representative genome browser view of corresponding WGBS and Dnmt1-TOP-seq libraries. WGBS track denotes DNA methylation of individual CpGs ranging from 0% to 100%, Dnmt1-TOP-seq tracks show sequencing read coverage values.

(D) Comparison of CpG modification profiles over genomic elements from WGBS, RRBS, and Dnmt1-TOP-seq datasets. Reads were counted per non-overlapping 2 kb windows.

(E) Heatmap comparing CpG island modification levels derived from WGBS, RRBS, and Dnmt1-TOP-seq datasets. Methylation shown as percent methylation of individual CpGs ranging from 0% to 100%, Dnmt1-TOP-seq denotes amount of identified CpG targets.

(F) Representative CpG modification profiles of *Sfi1* and *H1fnt* CpG islands in WT/En cells. Columns bars indicate Dnmt1-TOP-seq mean read coverage, ±SD. Blue lines denote smoothed Gaussian GLM fit profiles.

(G) Density scatterplots comparing Dnmt1-TOP-seq-identified target fraction in WT/En cells against WT WGBS methylation levels across genomic elements as shown. Density increases from blue (low) to dark red (high).

(H) Comparative enrichment analysis of genomic elements and regulatory features. The odds ratio indicates enriched (>1) or depleted (<1) genomic element phrases in *Dnmt1* WT or KO WGBS and *Dnmt1* WT/En Dnmt1-TOP-seq datasets.

(I) Comparison of Dnmt1-TOP-seq modification profiles against Dnmt3a and Dnmt3b ChIP-seq normalized profiles at LTR and satellite elements. Lines indicate unmodified (0%), low (<20%), intermediate (40%–60%) and highly modified (>80%) CpG modification categories.

showed strong enrichment across pathways associated with reproduction, meiotic nuclear division and cell cycle, meiotic chromosome pairing, and piRNA metabolic processes (Figure S7H; Table S6). Akin to previously validated *Sfi1* and *H1fnt*, genomic mapping further defined a subset of 36 meiosis-associated promoter CGIs, including the top-five candidates *Slc25a31*, *Sycp1*, *Ezhip*, *Fkbp6*, and *Btbd18* (Figure S11). This observation may point at DNMT1 involvement in germline gene regulation during early embryogenesis[44] (see in the following section).

In light of prior reports that noted significant flank-dependent CpG modification bias *in vitro* and *in cellulo*,[45] we conducted a CpG sequence-context analysis spanning the genomic areas of prominent DNMT1-catalysis, including the CGI shores/shelves and germline-associated promoters. Our study, however, found no significant flank enrichment in 7 bp windows centered at CpG sites (Figure S7i). A detailed atomic level analysis of the DNMT1-DNA complexes identified no direct contacts or other interactions of the N1580 residue with the bound DNA,[45] which makes it unlikely that the alanine substitution at this position would affect the flank sequence preferences. On the other hand, intracellular DNMT1 catalysis and the replication-dependent maintenance in particular are strongly controlled by regulatory factors and chromatin modifications. Hence, the lack of context sensitivity may reflect an extensive chromatin-level regulation, effectively masking any intrinsic DNA sequence preferences of the enzyme.

Chemical tracking of DNMT1 activity during mESC priming identifies methylation landscapes linked with germ line promoter CGIs

Having established an efficient Dnmt1-TOP-seq procedure in the context of a minimally perturbed methylome, we conducted a pilot study of changes in DNMT1 catalysis and global DNA methylation landscapes during naive-to-primed cell state transition in mESCs (Figure 4A). The engineered cell lines along with KO and WT controls were followed for 8 days after changing from 2i/LIF to LIF medium and subjecting aliquoted fractions every 2 days to azide labeling and DNA analysis as described earlier. As expected, HPLC/MS analysis of collected samples showed a gradual increase of genomic m^5C levels in all mESC lines, reaching a plateau on day 4 of cultivation in LIF medium (Figure 4B). In contrast to En/En and KO cells, the mono-allelic WT/En cell line exhibited methylation changes observed in the WT cells. The increase of the N_3-m^5C levels in the engineered cells saturated on day 4 as well, in line with the changes of the global m^5C levels (Figure 4C). During the reverse cell-state transition (LIF to 2I/LIF), administration of the kinase inhibitors resulted in a fast (day 2) drop in the DNMT1-directed labeling, indicating a minimal, if any, DNMT1 catalysis under 2i conditions. The decline of the m^5C levels, however, was more gradual as the accumulated methylation could not be immediately removed; the decay rate was consistent with passive DNA demethylation in the absence of methylation maintenance, although a certain contribution of active TET-dependent demethylation pathway cannot be excluded.

To determine the genome-wide distribution of CpG modification events during the priming transition, aliquots of the collected samples were subjected to RRBS and Dnmt1-TOP-seq analysis. RRBS analysis showed a similar increase of the global m^5C levels with a nearly full saturation by day 4, (Figure 4D; Figure S12A). This DNA methylation trend was apparent across a range of genomic features, including coding genes, TEs, *cis*-regulatory regions, and CGIs (Figure 4E; Figure S12B). The Dnmt1-TOP-seq datasets showed a high CpG-read specificity and reasonable consistency even in cells cultured with 2i (Figures S12C and S12D), with a roughly 10-fold lower genome tagging intensity as compared to the LIF-grown cells. The rise of the total number of unique DNMT1-tagged (identified) CpGs continued after day 4, as did the accumulated amounts of modified unique targets across chromosomes and genomic features (Figure 4F; Figures S12E and S12F).

Further comparison of the Dnmt1-TOP-seq and RRBS profiles across genomic features (Figure 4H; Figure S12G) showed a rather uniform rise in CpG modifications. In all cases, the RRBS profiles on day 4 and day 8 appeared coincident, while the DNMT signal did not show a full profile saturation on day 4. This trend was also evident across CGIs globally and at an individual CGI level of a meiosis-associated *Sfi1* promoter region (Figure 4I; Figure S12H) implying that full commitment of DNMT1 to maintain the DNA methylome is reached at a later phase of the mESC "priming." Notably, in contrast to Dnmt1-TOP-seq, RRBS profiles showed an inverse inflection polarity (element versus adjoining regions) across DNA repeats (LTR, satellite, LINE, and SINE), hinting at possible differences in DNMT1 modification kinetics at these regions (Figure 4H; Figure S12G).

Functional enrichment analysis across genomic elements revealed a slight increase in coding genes, introns, and SINEs, with the most prominent jump apparent in CGI shores and CGI shelves during the last stages of the priming transition (Figure 4G). Interestingly, the enrichment of satellite regions followed the opposite trend, implying active DNMT1 involvement in modification of centromeric and/or telomeric regions in naive state and reduced activity in subsequent steps of the priming transition.

Finally, we searched for groups of genes that DNMT1 may specifically regulate. We used C-means unsupervised clustering of promoter CGIs identified by Dnmt1-TOP-seq and compared them with RRBS data representing aggregate methylation by all DNMTs (Figures 5A and 5B; Figure S13, Tables S7, and S8). Six major patterns of CpG modification changes during the priming transition were identified: acute (cluster 1), progressive (cluster 2), intermediate (cluster 3), saturating (cluster 4), late (cluster 5), and inverse (cluster 6), which comprised CGIs with lost methylation levels. Subsequent GO analysis showed that promoters associated with genes involved in cyclic AMP (cAMP) metabolism (Figure S13A) were hypermodified, whereas CGIs associated with RNA metabolism and DNA replication were demethylated during early phases of the mESC state transition (Figure S13B). Notably, this DNA modification rearrangement was partially evident in the RRBS dataset as well (Figure S13B). Furthermore, in line with our previous findings (Figure S7H), the analysis unveiled a group of pathways associated with germ line gene promoter CGIs that were gradually modified over a whole duration of the mESC "priming," including

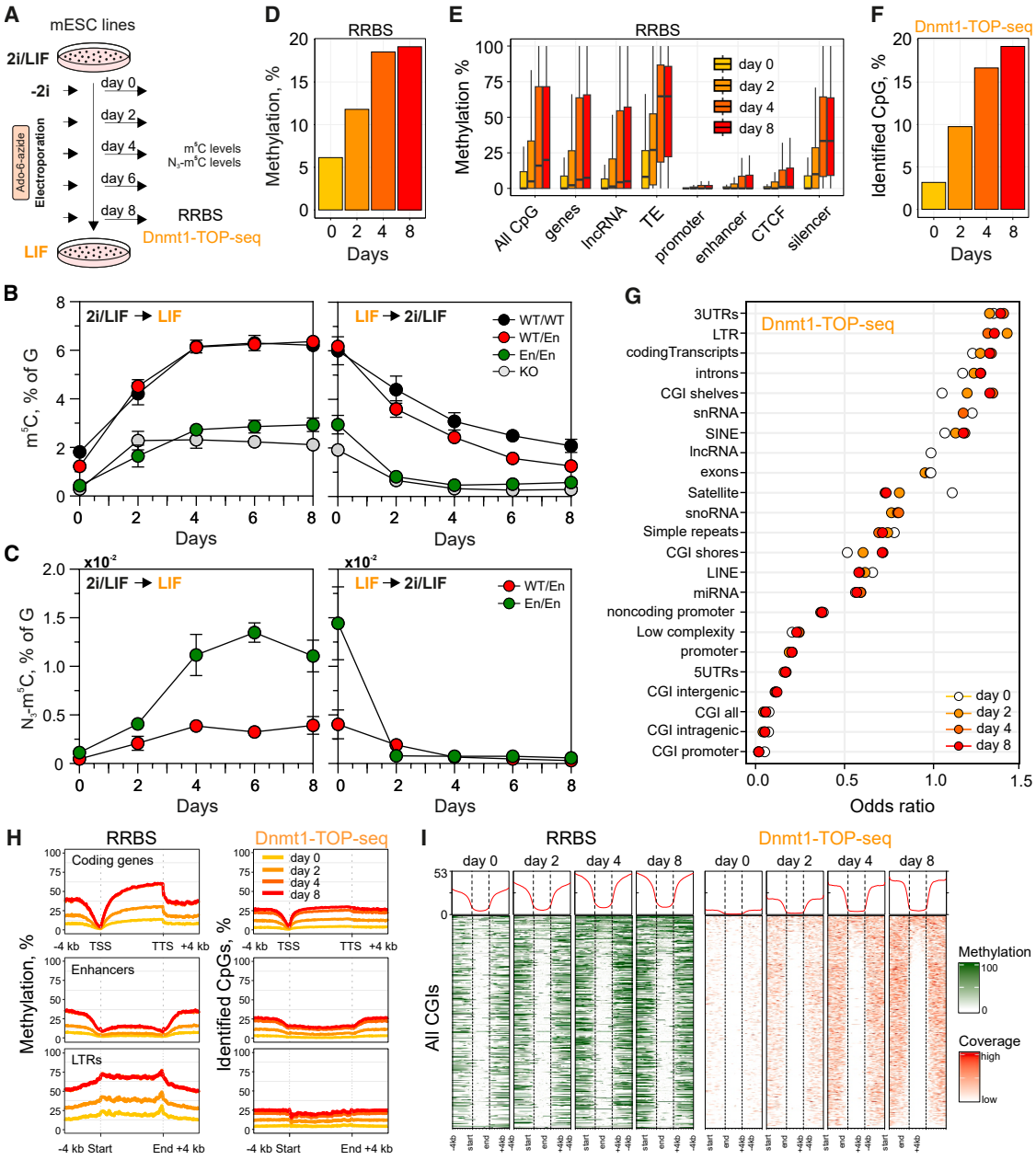

Figure 4. Chemical tracking of DNMT1 catalysis in mESCs during naive-to-primed transition

(A) Experimental workflow of mESC transition from naive ground state to primed cells. Cells were precultured in LIF cell medium supplemented with 2i inhibitors (2i/LIF) and then switched to LIF medium (day 0) samples were collected every two days until day 8. For LIF $\geq$ 2i/LIF transition, cells precultured in LIF medium were supplemented with 2i medium and samples were collected in 2-day intervals accordingly.

(B) HPLC-MS/MS analysis of genomic m^5C levels in mESC lines during the mESC state transition shown as (%) of dG. Dots denote mean ±SD, $n = 3$ independent experiments.

(C) HPLC-MS/MS analysis of DNMT1-specific cytosine modification N_3-m^5C in engineered mESCs after electroporation with 500 μM of Ado-6-azide. Dots denote mean ±SD, $n = 3$ independent experiments.

(D) Global CpG methylation dynamics in WT/En mESCs determined by RRBS analysis.

(E) CpG methylation distribution changes across genomic elements during the cellular state transition evaluated with RRBS. Lines indicate median, box is limited by the upper and lower quartiles, whiskers extend to 1.5*IQR.

(F) A fraction of unique CpGs (read start within 2 nt of a CpG) in WT/En mESCs identified by Dnmt1-TOP-seq during the 2i-to-LIF transition.

(legend continued on next page)

top DNMT1-targeted genes *Sycp1*, *Ezhip*, *Fkbp6*, and *Btbd18* (Figure 5A; Table S7). Notably, progressive changes in CpG modifications (cluster 2) were associated with the *Mael*, *Mei1*, *Syce3*, *Majin*, and *Tex11* genes involved in meiotic chromosome segregation. Likewise, cluster 3 exhibited intermediate accumulation of DNMT1-modified CGIs at genes associated with meiotic cell cycle and nuclear division, such as *Spo11*, *Tdrkh, Mov10L1*, and *Rpl10L*. This trend was not observed in the RRBS methylation data (Figure 5B), which mostly showed pathways linked to cellular differentiation. Since this difference could be due to a mismatch in the gene datasets used, we further inspected top pathways that were enriched with promoter CGIs at individual time points (Figures 5C and 5D; Figure S14A and Table S9). GO analysis demonstrated a comparable enrichment of terms related to germ line cell maintenance in both the Dnmt1-TOP-seq and RRBS libraries. Furthermore, RRBS DMR analysis further validated this observation showing that the most prominently methylated promoter CGIs on day 4 and day 8 (vs. day 0) are related to a similar set of cellular pathways (Figure S14).

DISCUSSION

Catalysis-based in-cell tracking of individual epigenetic writers has long been poorly accessible due to a lack of minimally invasive approaches for manipulating MTase activity in live cells. Prototype systems for AdoMet analog-based profiling of protein methylation targets in cell lysates[46] and for analysis of histone methylation[47] and mRNA adenine-*N*6 methylation[48,49] in transfected and/or methionine-deprived cells were described. However, in most cases the engineered proteins are produced inside cells by transfection on viral vectors, which unavoidably leads to high heterogeneity of the protein expression levels within a cell population. Moreover, the tagging activity of engineered MTases appears to be strongly suppressed in the presence of endogenous AdoMet, which typically requires methionine deprivation during analysis. Due to significant perturbations of key cellular parameters from *in vivo* homeostasis, such analyses were instrumental for general MTase target identification. In this study, we developed a genetically stable cellular system for selective tracking of the DNMT1 catalytic action with minimal disturbance of the cellular methylation homeostasis (including the levels of methionine, DNMT proteins, and DNA methylation). We also demonstrate that the distribution of CpG methylation in our mono-allelic engineered cells well mirrors that of the parental cells across genome-wide regions and regulatory elements (Figure 2) indicating that the methylation landscape is well preserved at least at the global level.

The primary role of DNMT1 as the maintenance methyltransferase is reflected in a general similarity of the Dnmt-TOP-seq and WGBS profiles. However, many differences can be observed across numerous genetic elements and features, which may relate to distinct behavior of DNMT1 in specific contexts. As mentioned earlier, some of these differences arise due to physical differences of the two sampling techniques, which can be eliminated to a certain degree using functional enrichment analysis. Moreover, the Dnmt-TOP-seq records the catalytic activity that is exerted during a defined time window (1–3 h). During this time, only current catalytic events are chemically tagged, as opposed to canonical m^5C profiling approaches including WGBS, which contain information from all previous and new events (steady state level). Given that the deposited azide tags are largely immune to TET-promoted oxidation and are unlikely to be removed in par with m^5C,[38] the DNMT-TOP-seq signal should be enriched at regions undergoing active methylation/demethylation.[39,40] To this end, we found that CGI shelves and shores as well as coding regions (Figure 3H) were significantly enriched in the DNMT1 modification profile as compared to the WGBS signal. Indeed, extensive TET-promoted demethylation of gene promoters and gene bodies in highly expressed genes has been reported in mESC.[41,42] In differentiated cells, TET1 was shown to prevent methylation spreading from methylated edges into CGIs.[50] Our data provide evidence in favor of this phenomenon occurring in mESCs as well with prominent DNMT1 catalytic activity at CGI boundaries in the primed state but not in the naive state (Figure 4G).

On the other hand, a noticeable drop in modified CpG enrichment at DNA repeat sequences (Figures 3H and 4G) point at complex dynamics of methylation maintenance. In particular, this may relate to the fact that DNMT1 cannot fully keep up with the pace of DNA replication in fast proliferating mESCs, leading to a bi-modal maintenance profile with rapid and replication-uncoupled slow phases[51–53]; the latter occurs at varying velocities across distinct genomic regions, correlating with the local CpG density. Moreover, DNMT1-specific activity inversely correlated with DNMT3B localization in satellite regions (Figure 3I; Figure S10) in line with previous findings that DNMT3B specializes in the methylation of centrosomic satellite repeats, which is essential for chromosome stability and proper segregation.[54]

However, despite the delayed methylation, a significantly reduced m^5C enrichment in the KO cells versus WT cells may point to important roles of DNMT1 catalysis at LTR and LINE repeats (Figure 3H). In fact, it has been reported that LTR, particularly IAP elements, are directly targeted by DNMT1 and retain methylation in DNMT3 DKO cells.[12,13] Further studies are required to fully delineate the mechanistic interplay underlying methylation of these genomic elements.

The 2i/LIF cell-state transition of mESCs is a well-exploited model for deciphering complex DNA methylation reprograming events.[30,34] Notably, the derived WT/En cell line exhibits faithful maintenance of CpG methylation during the cell-state transition closely resembling the pattern observed in WT cells, whereas intragenomic incorporation of N_3-m^5C occurs in a cell-state dependent manner (Figures 4B and 4C). In a fertilized mammalian cell containing two haploid pronuclei, the paternal and

(G) Enrichment analysis of genomic elements and regulatory features in WT/En cells. The odds ratio indicates an enriched (>1) or depleted (<1) genomic element phrase in the Dnmt1-TOP-seq dataset.
(H) CpG modification profiles over genomic sequences of coding genes, enhancers and LTRs in WT/En mESC in the RRBS and Dnmt1-TOP-seq datasets. Reads were counted per non-overlapping 2 kb windows.
(I) Heatmaps of CpG modification in CGIs obtained by RRBS or Dnmt1-TOP-seq during the cell state transition.

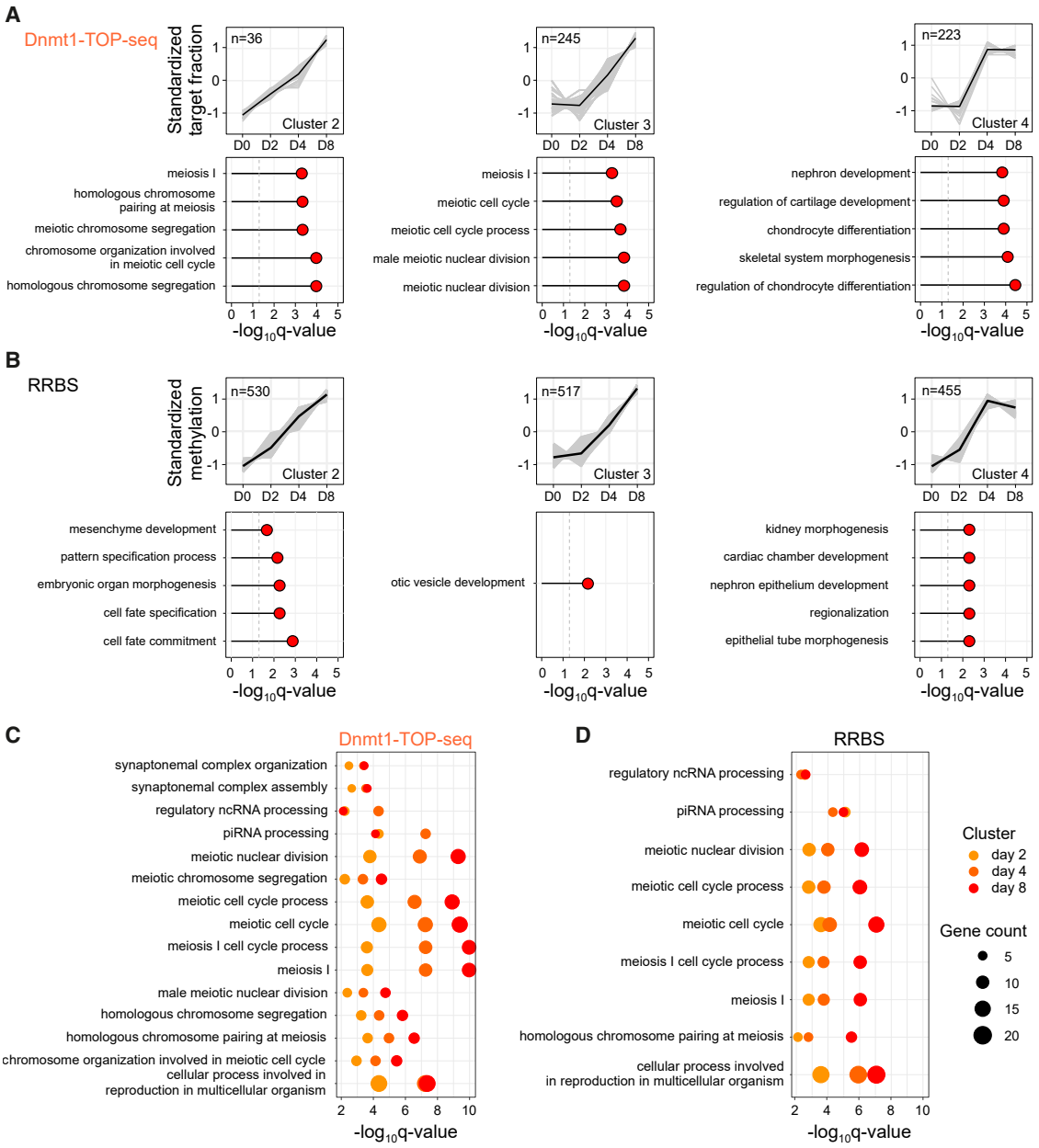

Figure 5. DNMT1 defines the methylation landscape of primordial gene CGIs during mESC priming

(A) C-means clustering of promoter CGI profiles with assigned top 5 GO terms. CGIs modification levels were evaluated using Dnmt1-TOP-seq in WT/En mESCs electroporated with 1 mM Ado-6-azide. Black lines represent mean profiles.

(B) GO term enrichment analysis of promoter CGIs grouped by C-means clustering evaluated with RRBS. Black lines represent mean profiles.

(C) GO term enrichment of genes with modified CGI promoters during each time point of 2i-to-LIF transition observed by Dnmt1-TOP-seq. CGIs with at least one modified CpG in all biological replicates were chosen for the analysis. q value denotes false discovery rate. Dot color transition depicts CGI profiling day, while dot size refers gene count.

(D) RRBS GO enrichment analysis of genes with methylated CGI promoters during the mESC priming transition. q-value denotes false discovery rate. Dot color denotes transition day; dot size - gene count.

maternal genomes undergo an extensive loss of epigenetic memory,[55] culminating in subsequent *de novo* remethylation during the implantation stage. A core subset of promoter CGIs undergoing such dynamic DNA methylation during early embryogenesis predominantly comprises pluripotency and developmental genes.[44] This is also corroborated by our RRBS and Dnmt1-TOP-seq data since both techniques revealed promoter modification enrichment in pathways associated with early cellular differentiation during the cell state transition (Figure 5). Remarkably, we find that DNMT1 is specifically

involved in the control of germline gene promoter CGIs, which strongly manifested itself upon cellular escape from the naive state (Figures 5A–5C), whereas these changes are hardly detectable in the RRBS data (Figures 5B–5D). The transition from naive to primed pluripotency involves an intermediate formative state that enables a critical fate bifurcation toward primordial germ cells (PGCs); this speciation is followed by DNA demethylation and subsequent development of germline-specific methylation patterns.[56,57] Primary germline-specific genes associated with late gametogenesis and meiosis predominantly display promoter or enhancer methylation and constitute the principal category of genes that are de-repressed in DNMT TKO cells during mESC "priming,"[58,59] underscoring DNA methylation as a key negative regulator of germline competence. Consistent with our observations, a recent study also indicated that the *de novo* activity of DNMT1 may contribute to the repression of primitive endoderm genes and the initiation of epiblast-like cells and mesendodermal differentiation,[60] although DNMT1 alone was insufficient to establish "primed" pluripotency or to repress germline-specific gene expression. Consequently, these data suggest that DNMT1 could play an integral role in regulating early lineage commitment beyond merely maintaining established DNA methylation.

In conclusion, we present here the development and thorough validation of a new analytic platform with unprecedented capacity to report on dynamic aspects of epigenetic processes by taking snapshots of the catalytic activity exerted during a define time window. Such temporal DNA modification mapping in realistic cell models gives a unique observation angle at DNMT-specific methylation that was unattainable using previous methods. This new approach is a valuable addition to the epigenomic toolbox and can be readily adapted for in-depth studies of a variety of cellular reprograming events including embryogenesis, development, and disease.

Limitations of the study

Applicability of this approach is constrained by obligatory genome editing to generate engineered cell lines and by physical limitations of electroporation techniques. The first issue is alleviated by rapid advances in genome editing technologies and profound structural conservation of catalytic residues in mammalian DNMTs. Electroporation can be combined with or replaced by metabolic in-cell production of the cofactors using engineered AdoMet synthetase (MAT2A)[61] paving the way to implementation of this platform in human and other vertebrate cells or even in organismal contexts. As mentioned earlier, only a fraction of all available target sites undergo labeling during an experimental time span in heterozygotic cells, and thus this temporal DNMT-specific "catalysome" is by definition distinct from the aggregate methylation signal shaped by the action of the three DNMT and three TET enzymes. Mapping of the tagged sites using TOP-seq technique gives semi-quantitative CpG modification profiles, which altogether makes their direct correlation with bisulfite sequencing-derived datasets rather cumbersome. These limitations can in part be overcome by enrichment analysis as demonstrated earlier or ultimately resolved by adaptation of the next-generation single-molecule sequencing for direct readout of the azide-tagged CpG sites. Yet, untangling DNMT-specific functional roles from just two types of datasets (DNMT1 and methylome) may still be tricky and of limited resolution but this could in principle be improved when DNMT3 catalysome profiling becomes available.

RESOURCE AVAILABILITY

Lead contact

Further information and reasonable requests for resources and reagents should be directed to and will be fulfilled by the lead contact, Saulius Klimašauskas (saulius.klimasauskas@bti.vu.lt).

Materials availability

Plasmids generated in this study will be made available upon request. Mouse cell lines generated in this study will be made available upon request.

Data and code availability

The WGBS, RRBS, and Dnmt1-TOP-seq data gathered during the present study have been deposited with the Gene Expression Omnibus (GEO) database under accession number GSE281224. The R scripts used for data analysis are accessible on Zenodo: https://doi.org/10.5281/zenodo.15853491. UCSC genome browser sessions can be found at https://genome.ucsc.edu/s/kotrynak/Dnmt1FootPrints. The publicly accessible mouse dnmt3a and dnmt3b ChIP-seq datasets can be found in the GEO database (GSE118785).

ACKNOWLEDGMENTS

We thank Martynas Malikėnas and Viktoras Masevičius for synthesis of the Ado-6-azide cofactor; Bernadeta Masiulionytė, Radvilas Bendorys, and Gabrielė Sužiedėlytė for experimental assistance. This work was funded by the Ministry of Education, Science and Sports of Lithuania "University Excellence Initiatives" grant 12-001-01-01-01/S-A-UEI-23-10 to S.K. and Research Council of Lithuania grant S-MIP-23-108 to V.S.

AUTHOR CONTRIBUTIONS

S.K. and G.V. conceived and supervised the study; V.S. and G.V. designed the study; V.S., L.G., and A.R. performed the experiments; K.K. performed bioinformatics analysis; V.S., K.K., and G.V. performed formal analysis; V.S. and S.K. wrote the manuscript; and all authors commented on the paper.

DECLARATION OF INTERESTS

G.V. and S.K. are inventors on licensed patents related to mTAG and TOP-seq technologies. S.K. is a scientific advisor for Tagomics Ltd. All other authors declare no competing interests.

STAR★METHODS

Detailed methods are provided in the online version of this paper and include the following:

- KEY RESOURCES TABLE
- EXPERIMENTAL MODEL
- METHOD DETAILS
  - Synthetic cofactor
  - Generation of mono-allelic mouse embryonic *Dnmt1* N1580A cells
  - Cell electroporation with Ado-6-azide
  - Quantitative HPLC-MS/MS
  - Preparation of Dnmt1-TOP-seq libraries
  - Preparation of WGBS libraries
  - Preparation of RRBS libraries
  - Processing of Dnmt1-TOP-seq data
  - Processing of WGBS and RRBS data
  - Reference genome annotation
  - Functional enrichment analysis

- Time-course data clustering
- Sanger bisulfite sequencing
- RT-qPCR
- Western blotting
- Statistical analysis

SUPPLEMENTAL INFORMATION

Supplemental information can be found online at https://doi.org/10.1016/j.celrep.2026.117435.

Received: October 9, 2025
Revised: March 28, 2026
Accepted: May 4, 2026
Published: June 4, 2026

REFERENCES

1. Jurkowska, R.Z., and Jeltsch, A. (2022). Enzymology of Mammalian DNA Methyltransferases. In DNA Methyltransferases - Role and Function, A. Jeltsch and R.Z. Jurkowska, eds. (Springer International Publishing), pp. 69–110. https://doi.org/10.1007/978-3-031-11454-0_4.
2. Tajima, S., Suetake, I., Takeshita, K., Nakagawa, A., Kimura, H., and Song, J. (2022). Domain Structure of the Dnmt1, Dnmt3a, and Dnmt3b DNA Methyltransferases. In DNA Methyltransferases - Role and Function, A. Jeltsch and R.Z. Jurkowska, eds. (Springer International Publishing), pp. 45–68. https://doi.org/10.1007/978-3-031-11454-0_3.
3. Kriaucionis, S., and Heintz, N. (2009). The Nuclear DNA Base 5-Hydroxymethylcytosine Is Present in Purkinje Neurons and the Brain. Science *324*, 929–930. https://doi.org/10.1126/science.1169786.
4. Tahiliani, M., Koh, K.P., Shen, Y., Pastor, W.A., Bandukwala, H., Brudno, Y., Agarwal, S., Iyer, L.M., Liu, D.R., Aravind, L., and Rao, A. (2009). Conversion of 5-Methylcytosine to 5-Hydroxymethylcytosine in Mammalian DNA by MLL Partner TET1. Science *324*, 930–935. https://doi.org/10.1126/science.1170116.
5. Kriukienė, E., Tomkuvienė, M., and Klimašauskas, S. (2024). 5-Hydroxymethylcytosine: the many faces of the sixth base of mammalian DNA. Chem. Soc. Rev. *53*, 2264–2283. https://doi.org/10.1039/d3cs00858d.
6. Denis, H., Ndlovu, M.N., and Fuks, F. (2011). Regulation of mammalian DNA methyltransferases: a route to new mechanisms. EMBO Rep. *12*, 647–656. https://doi.org/10.1038/embor.2011.110.
7. Chen, Z., and Zhang, Y. (2020). Role of Mammalian DNA Methyltransferases in Development. Annu. Rev. Biochem. *89*, 135–158. https://doi.org/10.1146/annurev-biochem-103019-102815.
8. Lee, H.J., Hore, T.A., and Reik, W. (2014). Reprogramming the Methylome: Erasing Memory and Creating Diversity. Cell Stem Cell *14*, 710–719. https://doi.org/10.1016/j.stem.2014.05.008.
9. Vilkaitis, G., Suetake, I., Klimašauskas, S., and Tajima, S. (2005). Processive Methylation of Hemimethylated CpG Sites by Mouse Dnmt1 DNA Methyltransferase. J. Biol. Chem. *280*, 64–72. https://doi.org/10.1074/jbc.M411126200.
10. Xu, Z., Shi, J., Chen, Q., Yang, S., Wang, Z., Xiao, B., Lai, Z., Jing, Y., Li, Y., and Li, X. (2025). Regulation of de novo and maintenance DNA methylation by DNA methyltransferases in postimplantation embryos. J. Biol. Chem. *301*, 107990. https://doi.org/10.1016/j.jbc.2024.107990.
11. Baubec, T., Colombo, D.F., Wirbelauer, C., Schmidt, J., Burger, L., Krebs, A.R., Akalin, A., and Schübeler, D. (2015). Genomic profiling of DNA methyltransferases reveals a role for DNMT3B in genic methylation. Nature *520*, 243–247. https://doi.org/10.1038/nature14176.
12. Haggerty, C., Kretzmer, H., Riemenschneider, C., Kumar, A.S., Mattei, A.L., Bailly, N., Gottfreund, J., Giesselmann, P., Weigert, R., Brändl, B., et al. (2021). Dnmt1 has de novo activity targeted to transposable elements. Nat. Struct. Mol. Biol. *28*, 594–603. https://doi.org/10.1038/s41594-021-00603-8.
13. Li, Z., Dai, H., Martos, S.N., Xu, B., Gao, Y., Li, T., Zhu, G., Schones, D.E., and Wang, Z. (2015). Distinct roles of DNMT1-dependent and DNMT1-independent methylation patterns in the genome of mouse embryonic stem cells. Genome Biol. *16*, 115. https://doi.org/10.1186/s13059-015-0685-2.
14. Scelfo, A., Barra, V., Abdennur, N., Spracklin, G., Busato, F., Salinas-Luypaert, C., Bonaiti, E., Velasco, G., Bonhomme, F., Chipont, A., et al. (2024). Tunable DNMT1 degradation reveals DNMT1/DNMT3B synergy in DNA methylation and genome organization. J. Cell Biol. *223*, e202307026. https://doi.org/10.1083/jcb.202307026.
15. Jones, P.A., and Liang, G. (2009). Rethinking how DNA methylation patterns are maintained. Nat. Rev. Genet. *10*, 805–811. https://doi.org/10.1038/nrg2651.
16. Liao, J., Karnik, R., Gu, H., Ziller, M.J., Clement, K., Tsankov, A.M., Akopian, V., Gifford, C.A., Donaghey, J., Galonska, C., et al. (2015). Targeted disruption of DNMT1, DNMT3A and DNMT3B in human embryonic stem cells. Nat. Genet. *47*, 469–478. https://doi.org/10.1038/ng.3258.
17. Cai, Y., Tsai, H.-C., Yen, R.-W.C., Zhang, Y.W., Kong, X., Wang, W., Xia, L., and Baylin, S.B. (2017). Critical threshold levels of DNA methyltransferase 1 are required to maintain DNA methylation across the genome in human cancer cells. Genome Res. *27*, 533–544. https://doi.org/10.1101/gr.208108.116.
18. Gu, T., Lin, X., Cullen, S.M., Luo, M., Jeong, M., Estecio, M., Shen, J., Hardikar, S., Sun, D., Su, J., et al. (2018). DNMT3A and TET1 cooperate to regulate promoter epigenetic landscapes in mouse embryonic stem cells. Genome Biol. *19*, 88. https://doi.org/10.1186/s13059-018-1464-7.
19. Ngan, K.C.-H., Hoenig, S.M., Kwok, H.S., Lue, N.Z., Gosavi, P.M., Tanner, D.A., Garcia, E.M., Lee, C., and Liau, B.B. (2023). Activity-based CRISPR scanning uncovers allostery in DNA methylation maintenance machinery. eLife *12*, e80640. https://doi.org/10.7554/eLife.80640.
20. Yamaguchi, K., Chen, X., Rodgers, B., Miura, F., Bashtrykov, P., Bonhomme, F., Salinas-Luypaert, C., Haxholli, D., Gutekunst, N., Aygenli, B.Ö., et al. (2024). Non-canonical functions of UHRF1 maintain DNA methylation homeostasis in cancer cells. Nat. Commun. *15*, 2960. https://doi.org/10.1038/s41467-024-47314-4.
21. Biniszkiewicz, D., Gribnau, J., Ramsahoye, B., Gaudet, F., Eggan, K., Humpherys, D., Mastrangelo, M.-A., Jun, Z., Walter, J., and Jaenisch, R. (2002). Dnmt1 Overexpression Causes Genomic Hypermethylation, Loss of Imprinting, and Embryonic Lethality. Mol. Cell Biol. *22*, 2124–2135. https://doi.org/10.1128/MCB.22.7.2124-2135.2002.
22. Elder, E., Lemieux, A., and McGraw, S. (2026). Mouse embryonic stem cells exhibit cancer-like DNA methylation landscapes upon DNMT1 overexpression. Preprint at bioRxiv. https://doi.org/10.64898/2026.01.26.701550.
23. Elder, E., Lemieux, A., Legault, L.-M., Caron, M., Bertrand-Lehouillier, V., Dupas, T., Raynal, N.J.-M., Bourque, G., Sinnett, D., Gévry, N., and McGraw, S. (2025). Rescuing DNMT1 fails to fully reverse the molecular and functional repercussions of its loss in mouse embryonic stem cells. Nucleic Acids Res. *53*, gkaf130. https://doi.org/10.1093/nar/gkaf130.
24. Ling, Y., Sankpal, U.T., Robertson, A.K., McNally, J.G., Karpova, T., and Robertson, K.D. (2004). Modification of de novo DNA methyltransferase 3a (Dnmt3a) by SUMO-1 modulates its interaction with histone deacetylases (HDACs) and its capacity to repress transcription. Nucleic Acids Res. *32*, 598–610. https://doi.org/10.1093/nar/gkh195.
25. Estève, P.-O., Chang, Y., Samaranayake, M., Upadhyay, A.K., Horton, J.R., Feehery, G.R., Cheng, X., and Pradhan, S. (2011). A methylation and phosphorylation switch between an adjacent lysine and serine determines human DNMT1 stability. Nat. Struct. Mol. Biol. *18*, 42–48. https://doi.org/10.1038/nsmb.1939.
26. Qin, W., Leonhardt, H., and Pichler, G. (2011). Regulation of DNA methyltransferase 1 by interactions and modifications. Nucleus *2*, 392–402. https://doi.org/10.4161/nucl.2.5.17928.
27. Li, B.-Z., Huang, Z., Cui, Q.-Y., Song, X.-H., Du, L., Jeltsch, A., Chen, P., Li, G., Li, E., and Xu, G.-L. (2011). Histone tails regulate DNA methylation by

allosterically activating de novo methyltransferase. Cell Res. *21*, 1172–1181. https://doi.org/10.1038/cr.2011.92.

28. Ying, Q.-L., Wray, J., Nichols, J., Batlle-Morera, L., Doble, B., Woodgett, J., Cohen, P., and Smith, A. (2008). The ground state of embryonic stem cell self-renewal. Nature *453*, 519–523. https://doi.org/10.1038/nature06968.

29. Sim, Y.-J., Kim, M.-S., Nayfeh, A., Yun, Y.-J., Kim, S.-J., Park, K.-T., Kim, C.-H., and Kim, K.-S. (2017). 2i Maintains a Naive Ground State in ESCs through Two Distinct Epigenetic Mechanisms. Stem Cell Rep. *8*, 1312–1328. https://doi.org/10.1016/j.stemcr.2017.04.001.

30. Marks, H., Kalkan, T., Menafra, R., Denissov, S., Jones, K., Hofemeister, H., Nichols, J., Kranz, A., Stewart, A.F., Smith, A., and Stunnenberg, H.G. (2012). The Transcriptional and Epigenomic Foundations of Ground State Pluripotency. Cell *149*, 590–604. https://doi.org/10.1016/j.cell.2012.03.026.

31. von Meyenn, F., Iurlaro, M., Habibi, E., Liu, N.Q., Salehzadeh-Yazdi, A., Santos, F., Petrini, E., Milagre, I., Yu, M., Xie, Z., et al. (2016). Impairment of DNA Methylation Maintenance Is the Main Cause of Global Demethylation in Naive Embryonic Stem Cells. Mol. Cell *62*, 848–861. https://doi.org/10.1016/j.molcel.2016.04.025.

32. Stankevičius, V., Gibas, P., Masiulionytė, B., Gasiulė, L., Masevičius, V., Klimašauskas, S., and Vilkaitis, G. (2022). Selective chemical tracking of Dnmt1 catalytic activity in live cells. Mol. Cell *82*, 1053–1065.e1058. https://doi.org/10.1016/j.molcel.2022.02.008.

33. Anzalone, A.V., Randolph, P.B., Davis, J.R., Sousa, A.A., Koblan, L.W., Levy, J.M., Chen, P.J., Wilson, C., Newby, G.A., Raguram, A., and Liu, D.R. (2019). Search-and-replace genome editing without double-strand breaks or donor DNA. Nature *576*, 149–157. https://doi.org/10.1038/s41586-019-1711-4.

34. Habibi, E., Brinkman, A.B., Arand, J., Kroeze, L.I., Kerstens, H.H.D., Matarese, F., Lepikhov, K., Gut, M., Brun-Heath, I., Hubner, N.C., et al. (2013). Whole-Genome Bisulfite Sequencing of Two Distinct Interconvertible DNA Methylomes of Mouse Embryonic Stem Cells. Cell Stem Cell *13*, 360–369. https://doi.org/10.1016/j.stem.2013.06.002.

35. Leitch, H.G., McEwen, K.R., Turp, A., Encheva, V., Carroll, T., Grabole, N., Mansfield, W., Nashun, B., Knezovich, J.G., Smith, A., et al. (2013). Naive pluripotency is associated with global DNA hypomethylation. Nat. Struct. Mol. Biol. *20*, 311–316. https://doi.org/10.1038/nsmb.2510.

36. Wu, B., Li, Y., Li, B., Zhang, B., Wang, Y., Li, L., Gao, J., Fu, Y., Li, S., Chen, C., et al. (2021). DNMTs Play an Important Role in Maintaining the Pluripotency of Leukemia Inhibitory Factor-Dependent Embryonic Stem Cells. Stem Cell Rep. *16*, 582–596. https://doi.org/10.1016/j.stemcr.2021.01.017.

37. Staševskij, Z., Gibas, P., Gordevičius, J., Kriukienė, E., and Klimašauskas, S. (2017). Tethered Oligonucleotide-Primed Sequencing, TOP-Seq: A High-Resolution Economical Approach for DNA Epigenome Profiling. Mol. Cell *65*, 554–564.e556. https://doi.org/10.1016/j.molcel.2016.12.012.

38. Tomkuvienė, M., Ikasalaitė, D., Slyvka, A., Rukšėnaitė, A., Ravichandran, M., Jurkowski, T.P., Bochtler, M., and Klimašauskas, S. (2020). Enzymatic Hydroxylation and Excision of Extended 5-Methylcytosine Analogues. J. Mol. Biol. *432*, 6157–6167. https://doi.org/10.1016/j.jmb.2020.10.011.

39. Spada, F., Schiffers, S., Kirchner, A., Zhang, Y., Arista, G., Kosmatchev, O., Korytiakova, E., Rahimoff, R., Ebert, C., and Carell, T. (2020). Active turnover of genomic methylcytosine in pluripotent cells. Nat. Chem. Biol. *16*, 1411–1419. https://doi.org/10.1038/s41589-020-0621-y.

40. Ginno, P.A., Gaidatzis, D., Feldmann, A., Hoerner, L., Imanci, D., Burger, L., Zilbermann, F., Peters, A.H.F.M., Edenhofer, F., Smallwood, S.A., et al. (2020). A genome-scale map of DNA methylation turnover identifies site-specific dependencies of DNMT and TET activity. Nat. Commun. *11*, 2680. https://doi.org/10.1038/s41467-020-16354-x.

41. Xu, Y., Wu, F., Tan, L., Kong, L., Xiong, L., Deng, J., Barbera, A.J., Zheng, L., Zhang, H., Huang, S., et al. (2011). Genome-wide Regulation of 5hmC, 5mC, and Gene Expression by Tet1 Hydroxylase in Mouse Embryonic Stem Cells. Mol. Cell *42*, 451–464. https://doi.org/10.1016/j.molcel.2011.04.005.

42. Rasmussen, K.D., and Helin, K. (2016). Role of TET enzymes in DNA methylation, development, and cancer. Genes Dev. *30*, 733–750. https://doi.org/10.1101/gad.276568.115.

43. Weinberg, D.N., Papillon-Cavanagh, S., Chen, H., Yue, Y., Chen, X., Rajagopalan, K.N., Horth, C., McGuire, J.T., Xu, X., Nikbakht, H., et al. (2019). The histone mark H3K36me2 recruits DNMT3A and shapes the intergenic DNA methylation landscape. Nature *573*, 281–286. https://doi.org/10.1038/s41586-019-1534-3.

44. Borgel, J., Guibert, S., Li, Y., Chiba, H., Schübeler, D., Sasaki, H., Forné, T., and Weber, M. (2010). Targets and dynamics of promoter DNA methylation during early mouse development. Nat. Genet. *42*, 1093–1100. https://doi.org/10.1038/ng.708.

45. Adam, S., Anteneh, H., Hornisch, M., Wagner, V., Lu, J., Radde, N.E., Bashtrykov, P., Song, J., and Jeltsch, A. (2020). DNA sequence-dependent activity and base flipping mechanisms of DNMT1 regulate genome-wide DNA methylation. Nat. Commun. *11*, 3723. https://doi.org/10.1038/s41467-020-17531-8.

46. Sohtome, Y., and Sodeoka, M. (2018). Development of Chaetocin and S-Adenosylmethionine Analogues as Tools for Studying Protein Methylation. Chem. Rec. *18*, 1660–1671. https://doi.org/10.1002/tcr.201800118.

47. Wang, R., Islam, K., Liu, Y., Zheng, W., Tang, H., Lailler, N., Blum, G., Deng, H., and Luo, M. (2013). Profiling Genome-Wide Chromatin Methylation with Engineered Posttranslation Apparatus within Living Cells. J. Am. Chem. Soc. *135*, 1048–1056. https://doi.org/10.1021/ja309412s.

48. Hartstock, K., Nilges, B.S., Ovcharenko, A., Cornelissen, N.V., Püllen, N., Lawrence-Dörner, A.-M., Leidel, S.A., and Rentmeister, A. (2018). Enzymatic or In Vivo Installation of Propargyl Groups in Combination with Click Chemistry for the Enrichment and Detection of Methyltransferase Target Sites in RNA. Angew. Chem. Int. Ed. Engl. *57*, 6342–6346. https://doi.org/10.1002/anie.201800188.

49. Shu, X., Cao, J., Cheng, M., Xiang, S., Gao, M., Li, T., Ying, X., Wang, F., Yue, Y., Lu, Z., et al. (2020). A metabolic labeling method detects m6A transcriptome-wide at single base resolution. Nat. Chem. Biol. *16*, 887–895. https://doi.org/10.1038/s41589-020-0526-9.

50. Jin, C., Lu, Y., Jelinek, J., Liang, S., Estecio, M.R.H., Barton, M.C., and Issa, J.-P.J. (2014). TET1 is a maintenance DNA demethylase that prevents methylation spreading in differentiated cells. Nucleic Acids Res. *42*, 6956–6971. https://doi.org/10.1093/nar/gku372.

51. Charlton, J., Downing, T.L., Smith, Z.D., Gu, H., Clement, K., Pop, R., Akopian, V., Klages, S., Santos, D.P., Tsankov, A.M., et al. (2018). Global delay in nascent strand DNA methylation. Nat. Struct. Mol. Biol. *25*, 327–332. https://doi.org/10.1038/s41594-018-0046-4.

52. Ming, X., Zhang, Z., Zou, Z., Lv, C., Dong, Q., He, Q., Yi, Y., Li, Y., Wang, H., and Zhu, B. (2020). Kinetics and mechanisms of mitotic inheritance of DNA methylation and their roles in aging-associated methylome deterioration. Cell Res. *30*, 980–996. https://doi.org/10.1038/s41422-020-0359-9.

53. Nishiyama, A., Mulholland, C.B., Bultmann, S., Kori, S., Endo, A., Saeki, Y., Qin, W., Trummer, C., Chiba, Y., Yokoyama, H., et al. (2020). Two distinct modes of DNMT1 recruitment ensure stable maintenance DNA methylation. Nat. Commun. *11*, 1222. https://doi.org/10.1038/s41467-020-15006-4.

54. Xu, G.-L., Bestor, T.H., Bourc'his, D., Hsieh, C.-L., Tommerup, N., Bugge, M., Hulten, M., Qu, X., Russo, J.J., and Viegas-Péquignot, E. (1999). Chromosome instability and immunodeficiency syndrome caused by mutations in a DNA methyltransferase gene. Nature *402*, 187–191. https://doi.org/10.1038/46052.

55. Smith, Z.D., Chan, M.M., Mikkelsen, T.S., Gu, H., Gnirke, A., Regev, A., and Meissner, A. (2012). A unique regulatory phase of DNA methylation in the early mammalian embryo. Nature *484*, 339–344. https://doi.org/10.1038/nature10960.

56. Seisenberger, S., Andrews, S., Krueger, F., Arand, J., Walter, J., Santos, F., Popp, C., Thienpont, B., Dean, W., and Reik, W. (2012). The Dynamics of Genome-wide DNA Methylation Reprogramming in Mouse Primordial Germ Cells. Mol. Cell *48*, 849–862. https://doi.org/10.1016/j.molcel.2012.11.001.

57. Smith, A. (2017). Formative pluripotency: the executive phase in a developmental continuum. Development *144*, 365–373. https://doi.org/10.1242/dev.142679.

58. Karimi, M.M., Goyal, P., Maksakova, I.A., Bilenky, M., Leung, D., Tang, J.X., Shinkai, Y., Mager, D.L., Jones, S., Hirst, M., and Lorincz, M.C. (2011). DNA Methylation and SETDB1/H3K9me3 Regulate Predominantly Distinct Sets of Genes, Retroelements, and Chimeric Transcripts in mESCs. Cell Stem Cell *8*, 676–687. https://doi.org/10.1016/j.stem.2011.04.004.

59. Schulz, M., Teissandier, A., De La Mata Santaella, E., Armand, M., Iranzo, J., El Marjou, F., Gestraud, P., Walter, M., Kinston, S., Göttgens, B., et al. (2024). DNA methylation restricts coordinated germline and neural fates in embryonic stem cell differentiation. Nat. Struct. Mol. Biol. *31*, 102–114. https://doi.org/10.1038/s41594-023-01162-w.

60. Ito, T., Kubiura-Ichimaru, M., Miura, F., Tajima, S., Surani, M.A., Ito, T., Yamaguchi, S., and Tada, M. (2024). DNMT1 can induce primary germ layer differentiation through de novo DNA methylation. Genes Cells *29*, 549–566. https://doi.org/10.1111/gtc.13130.

61. Gasiulė, L., Stankevičius, V., Kvederavičiūtė, K., Rimšelis, J.M., Klimkevičius, V., Petraitytė, G., Rukšėnaitė, A., Masevičius, V., and Klimašauskas, S. (2024). Engineered Methionine Adenosyltransferase Cascades for Metabolic Labeling of Individual DNA Methylomes in Live Cells. J. Am. Chem. Soc. *146*, 18722–18729. https://doi.org/10.1021/jacs.4c06529.

62. Malikėnas, M., Masevičius, V., and Klimašauskas, S. (2023). Synthesis of S-Adenosyl-L-Methionine Analogs with Extended Transferable Groups for Methyltransferase-Directed Labeling of DNA and RNA. Curr. Protoc. *3*, e799. https://doi.org/10.1002/cpz1.799.

63. Martin, M. (2011). Cutadapt removes adapter sequences from high-throughput sequencing reads. EMBnet J. *17*, 3. https://doi.org/10.14806/ej.17.1.200.

64. Li, H. (2013). Aligning sequence reads, clone sequences and assembly contigs with BWA-MEM. Preprint at arXiv. https://doi.org/10.48550/arXiv.1303.3997.

65. Danecek, P., Bonfield, J.K., Liddle, J., Marshall, J., Ohan, V., Pollard, M.O., Whitwham, A., Keane, T., McCarthy, S.A., Davies, R.M., and Li, H. (2021). Twelve years of SAMtools and BCFtools. GigaScience *10*, giab008. https://doi.org/10.1093/gigascience/giab008.

66. Lawrence, M., Huber, W., Pagès, H., Aboyoun, P., Carlson, M., Gentleman, R., Morgan, M.T., and Carey, V.J. (2013). Software for Computing and Annotating Genomic Ranges. PLoS Comput. Biol. *9*, e1003118. https://doi.org/10.1371/journal.pcbi.1003118.

67. Morgan, M., Anders, S., Lawrence, M., Aboyoun, P., Pagès, H., and Gentleman, R. (2009). ShortRead: a bioconductor package for input, quality assessment and exploration of high-throughput sequence data. Bioinformatics *25*, 2607–2608. https://doi.org/10.1093/bioinformatics/btp450.

68. Wickham, H., François, R., Henry, L., Müller, K., and Vaughan, D. (2023). dplyr: a grammar of data manipulation. R package version 1.1. 2. Computer software.

69. Morgan, M., Pages, H., Obenchain, V., and Hayden, N. (2016). Rsamtools: Binary alignment (BAM), FASTA, variant call (BCF), and tabix file import. R package version *1*, 677–689.

70. Krueger, F., and Andrews, S.R. (2011). Bismark: a flexible aligner and methylation caller for Bisulfite-Seq applications. Bioinformatics *27*, 1571–1572. https://doi.org/10.1093/bioinformatics/btr167.

71. Cavalcante, R.G., and Sartor, M.A. (2017). annotatr: genomic regions in context. Bioinformatics *33*, 2381–2383. https://doi.org/10.1093/bioinformatics/btx183.

72. Gu, Z., Eils, R., Schlesner, M., and Ishaque, N. (2018). EnrichedHeatmap: an R/Bioconductor package for comprehensive visualization of genomic signal associations. BMC Genom. *19*, 234. https://doi.org/10.1186/s12864-018-4625-x.

73. Gu, Z., and Hübschmann, D. (2021). Make Interactive Complex Heatmaps in R. Bioinformatics *38*, 1460–1462. https://doi.org/10.1093/bioinformatics/btab806.

74. Wu, T., Hu, E., Xu, S., Chen, M., Guo, P., Dai, Z., Feng, T., Zhou, L., Tang, W., Zhan, L., et al. (2021). clusterProfiler 4.0: A universal enrichment tool for interpreting omics data. Innovation *2*, 100141. https://doi.org/10.1016/j.xinn.2021.100141.

75. Kumar, L., and E Futschik, M. (2007). Mfuzz: a software package for soft clustering of microarray data. Bioinformation *2*, 5–7. https://doi.org/10.6026/97320630002005.

76. Frankish, A., Diekhans, M., Ferreira, A.M., Johnson, R., Jungreis, I., Loveland, J., Mudge, J.M., Sisu, C., Wright, J., Armstrong, J., et al. (2019). GENCODE reference annotation for the human and mouse genomes. Nucleic Acids Res. *47*, D766–D773. https://doi.org/10.1093/nar/gky955.

77. Dreos, R., Ambrosini, G., Périer, R.C., and Bucher, P. (2014). The Eukaryotic Promoter Database: expansion of EPDnew and new promoter analysis tools. Nucleic Acids Res. *43*, D92–D96. https://doi.org/10.1093/nar/gku1111.

78. Gao, T., and Qian, J. (2020). EnhancerAtlas 2.0: an updated resource with enhancer annotation in 586 tissue/cell types across nine species. Nucleic Acids Res. *48*, D58–D64. https://doi.org/10.1093/nar/gkz980.

79. Rohde, C., Zhang, Y., Reinhardt, R., and Jeltsch, A. (2010). BISMA - Fast and accurate bisulfite sequencing data analysis of individual clones from unique and repetitive sequences. BMC Bioinf. *11*, 230. https://doi.org/10.1186/1471-2105-11-230.

STAR★METHODS

KEY RESOURCES TABLE

REAGENT or RESOURCE	SOURCE	IDENTIFIER
Antibodies		
Rabbit polyclonal anti-DNMT1	Abcam	Cat#ab87654; RRID: AB_2041077
Mouse monoclonal anti-UHRF1 (H-8)	Santa Cruz	Cat#sc-373750; RRID: AB_10947236
Mouse monoclonal anti-DNMT3A (A-10)	Santa Cruz	Cat#sc-373905; RRID: AB_10920404
Mouse monoclonal anti-GAPDH (6C5)	Santa Cruz	Cat#sc-32233; RRID: AB_627679
Rabbit polyclonal anti-DNMT3B	Invitrogen	Cat#PA1-884; RRID: AB_2277463
Goat anti-Mouse IgG (H + L) Secondary Antibody, HRP	Invitrogen	Cat#31430
Goat anti-Rabbit IgG (H + L) Secondary Antibody, HRP	Invitrogen	Cat#31460
Chemicals, peptides, and recombinant proteins		
Ado-6-azide	Malikenas et al.[62]	N/A
Gelatin	Sigma-Aldrich	Cat#G1890
Trypsin-EDTA	Gibco	Cat#15400-054
Dulbecco's modified Eagle's medium	Gibco	Cat#11960-044
Embryonic stem cell FBS	Gibco	Cat#16141-079
Penicillin-Streptomycin	Gibco	Cat#15140-122
Sodium pyruvate	Gibco	Cat#11360-070
β-mercaptoethanol	Gibco	Cat#21985-023
GlutaMAX	Gibco	Cat#35050-061
MEM Non-essential amino acids	Gibco	Cat#11140-050
Mouse leukemia inhibitory factor	EMD Millipore	Cat#ESG1106
CHIR99021	Sigma-Aldrich	Cat#SML1046
PD0325901	Sigma-Aldrich	Cat#PZ0162
Opti-MEM	Gibco	Cat#11058-021
Lipofectamine LTX	Invitrogen	Cat#15338100
Puromycin	Sigma-Aldrich	Cat#P8833
FastDigest Eco31I	Thermo Fisher Scientific	Cat#FD0293
FastDigest BpiI	Thermo Fisher Scientific	Cat#FD1014
SatI restriction enzyme	Thermo Fisher Scientific	Cat#ER1641
Phire Tissue Direct PCR Master Mix	Thermo Fisher Scientific	Cat#F170L
FastAP Thermosensitive Alkaline Phosphatase	Thermo Fisher Scientific	Cat#EF0654
T4 PNK	Thermo Fisher Scientific	Cat#EK0032
T4 DNA Ligase	Thermo Fisher Scientific	Cat#EL0011
Halt™ Protease Inhibitor Cocktail	Thermo Fisher Scientific	Cat#87786
SuperSignal West Pico PLUS Chemiluminescent Substrate	Thermo Fisher Scientific	Cat#34580
Deposited data		
Dnmt-TOP-seq data, E14TG2a Dnmt1$^{WT/N1580A}$	This work	GEO: GSE281224
WGBS data	This work	GEO: GSE281224
RRBS data	This work	GEO: GSE281224
Dnmt-TOP-seq data, E14TG2a Dnmt1$^{N1580A/N1580A}$	Stankevicius et al.[32]	GEO: GSE182445
ChIP-seq data for Dnmt3a1 and Dnmt3b	Weinberg et al.[43]	GEO: GSE118785

(*Continued on next page*)

Continued

REAGENT or RESOURCE	SOURCE	IDENTIFIER
Experimental models: Cell lines		
Mouse embryonic stem cells, E14TG2a	ATCC	CRL-1821
Mouse embryonic stem cells, E14TG2a *Dnmt1*$^{WT/N1580A}$	This work	N/A
Mouse embryonic stem cells, E14TG2a *Dnmt1*$^{N1580A/N1580A}$	Stankevicius et al.[32]	N/A
Mouse embryonic stem cells, E14TG2a *Dnmt1* KO	Stankevicius et al.[32]	N/A
Oligonucleotides		
Oligonucleotides used for generation of KI mouse embryonic stem cells, see Table S1	Metabion	N/A
Oligonucleotides used for Dnmt1-TOP library preparation, see Table S2	Metabion	N/A
Biotinylated alkyne-containing DNA oligonucleotide, 5'-TXTTTTGTGTGGTTTGGAGA CTGACTACCAGATGT AACA-Biotin; X = C8-Alkyne-dT	BaseClick	N/A
Complementary priming strand with custom LNA modifications and phosphorothioate linkages at the 3′ end, 5'-TGTTACATCTGGTAGTCAGTCTCCAAACCACACAA	Exiqon	N/A
Primers used to amplify bisulfite-treated genomic DNA templates, see Table S3	Metabion	N/A
Primers used for qPCR analysis, see Table S4	Metabion	N/A
Recombinant DNA		
PE2-T2A-Puro	Gasiule et al.[61]	N/A
pU6-pegRNA-GG-acceptor	Anzalone et al.[33]	Addgene Cat#132777
phU6-gRNA	Anzalone et al.[33]	Addgene Cat#53188
Software and algorithms		
Cutadapt (4.4)	Martin[63]	https://cutadapt.readthedocs.io
R 4.3.0	R project	https://www.r-project.org/
BWA MEM	Li[64]	https://bio-bwa.sourceforge.net/
Samtools	Danecek et al.[65]	https://www.htslib.org/
GenomicRanges	Lawrence et al.[66]	https://bioconductor.org/packages/release/bioc/html/GenomicRanges.html
Data table	N/A	(https://github.com/Rdatatable/data.table
ShortRead	Morgan et al.[67]	https://bioconductor.org/packages/release/bioc/html/ShortRead.html
Dplyr	Wickham et al.[68]	https://dplyr.tidyverse.org/
Rsamtools	Morgan et al.[69]	https://github.com/Bioconductor/Rsamtools
gUtils	N/A	https://github.com/mskilab-org/gUtils
Bismark 0.22.3	Krueger and Andrews[70]	https://github.com/FelixKrueger/Bismark
annotatr	Cavalcante and Sartor[71]	https://bioconductor.org/packages/release/bioc/html/annotatr.html
MethylDackel 0.5.0	N/A	https://github.com/dpryan79/MethylDackel
EnrichedHeatmap	Gu et al.[72]	https://github.com/jokergoo/EnrichedHeatmap
ComplexHeatmap	Gu and Hübschmann[73]	https://jokergoo.github.io/ComplexHeatmap-reference/book/
clusterProfiler	Wu et al.[74]	https://github.com/YuLab-SMU/clusterProfiler

(*Continued on next page*)

Continued

REAGENT or RESOURCE	SOURCE	IDENTIFIER
M-fuzz	Kumar and Futschik[75]	https://bioc.r-universe.dev/Mfuzz
Data analysis scripts	This work	https://doi.org/10.5281/zenodo.15853491

EXPERIMENTAL MODEL

Mouse embryonic stem E14TG2a cell line was purchased from the American Type Culture Collection of Authenticated Cell Cultures (ATCC CRL-1821). Cells were grown on 0.15% gelatin-coated dishes in Dulbecco's modified Eagle's medium (DMEM; Gibco, USA) containing 15% fetal bovine serum (Gibco, USA), 1× penicillin/streptomycin (Gibco, USA), 0.1 mM sodium pyruvate (Gibco, China), 0.1 mM 2-mercaptoethanol (Gibco, USA), 1 mM L-alanyl-L-glutamine (Gibco, Japan), 1× non-essential amino acids (NEAA; Gibco, USA), 1000 U/ml mouse leukemia inhibitory factor (mLIF; Millipore, Germany), 3 μM CHIR99021 (Sigma-Aldrich, USA) and 1 μM PD0325901 (Sigma-Aldrich, USA) or in serum media without 2i.

For the cell state transition to LIF, cells cultivated in serum/LIF media with 2i were plated in the medium devoid of kinase inhibitors and cultured for subsequent 8 days, with cell passaging occurring in fresh medium at 48-h intervals. During the shift of mESC from LIF to 2i/LIF state, a precisely opposite cell passaging was maintained.

METHOD DETAILS

Synthetic cofactor

Ado-6-azide cofactor was chemically synthesized from AdoHcy as a mixture of *R,S*- and *S,S*-stereomers as previously described.[62]

Generation of mono-allelic mouse embryonic *Dnmt1* N1580A cells

Mono-allelic *Dnmt1*$^{wt/N1580A}$ E14TG2a cell line was generated using Search-and-replace genome editing PE3 strategy as described previously.[33] pegRNAs and sgRNA were prepared as follows: 10 μM of complementary single stranded pegRNA and sgRNA oligonucleotides (Metabion) were phosphorylated with 5 U T4 PNK (Thermo Fisher Scientific) in PNK buffer supplemented with 1 mM of ATP at 37°C for 30 min, denatured at 95°C for 5 min and annealed at cooling rate of 0.1°C/s pegRNA sequences were cloned into pU6-pegRNA-GG-acceptor (Addgene #132777) incubating 2.5 nM of annealed oligonucleotides, 30 ng of vector, 5 U FastDigest Eco31I (Thermo Fisher Scientific) and 5 U T4 DNA ligase (Thermo Fisher Scientific) in ligase buffer at 37°C for 5 min followed by incubation at 22°C for 5 min, repeating the reactions for 6 cycles. sgRNA oligonucleotides were cloned into phU6-gRNA (Addgene #53188) at BpiI sites.

A PE3 vector mixture was prepared in 25 μL of Opti-MEM medium (Gibco) containing 750 ng of PE2-T2A-Puro, 250 ng of pegRNA and 100 ng of sgRNA plasmids. 7.5×10^4 E14TG2a cells were transfected with the mixture using Lipofectamine LTX (Invitrogen) according to the manufacturer's instructions using reverse transfection. After 48 h, transfected cells were treated with 2 μg/mL puromycin for two days and plated for clonal expansion via serial dilution into individual gelatin-coated wells in 96-well plates. After single clone expansion, 1×10^5 cells of each clone were collected and screened by direct PCR using a Phire Tissue Direct PCR Master Mix and SatI (Thermo Fisher Scientific) restriction analysis according to manufacturer's recommendations to detect N1580A substitution. Genome editing in the *Dnmt1* coding sequence of selected clones was verified by Sanger sequencing. Single stranded pegRNA and sgRNA oligonucleotides and primer sequences are listed in Table S1.

Cell electroporation with Ado-6-azide

Cells were plated in 24-well plates at a density of 5×10^4 cells per well and grown for 48 h. Then, each well was washed twice with Opti-MEM medium (Thermo Fisher Scientific) and inoculated with freshly prepared 300 μL of 0.5–1 mM Ado-6-azide solution in Opti-MEM medium and electroporated using a NEPA21 electroporator (Nepa Gene) fitted with a cell culture plate electrode CUY900 at a cell poring pulse voltage of 200 V and a pulse duration of 5 ms. After electroporation, cells were incubated for 25 min at 37°C, washed with Opti-MEM, covered with fresh mESC medium, and incubated for a further 3 h. Cell pellets from each sample were harvested and stored at −20°C. gDNA was isolated as described.[32]

Quantitative HPLC-MS/MS

gDNA was enzymatically digested to nucleosides and analyzed on an integrated HPLC/ESI-MS/MS system (Agilent 1290 Infinity/6410 Triple Quad LC/MS) equipped with a Supelco Discovery HS C18 column as described.[32] Standard curves for m^5dC, dC, dG, dT, dA were established utilizing FastAP-treated 5′-nucleotides (Thermo Fisher Scientific). Calibration of N_3-m^5dC was carried out using an enzymatically modified 25-mer oligonucleotide as described.[32] All signals were adjusted to dG to account for variances in DNA input. MS data were examined using Agilent MassHunter software.

Preparation of Dnmt1-TOP-seq libraries

Dnmt1-TOP-seq libraries were prepared as described.[32] Primer sequences are listed in Table S2.

Preparation of WGBS libraries

100 ng of genomic DNA was bisulfite converted using Zymo EZ DNA Methylation-Lightning Kit according to the manufacturer's protocol. This was followed by a second strand synthesis reaction and then addition of adapters through tagmentation using Illumina's Nextera kit. PCR was performed with Illumina Nextera Unique Dual Indices. Library quality control was performed on the Agilent 2200 TapeStation. Libraries were sequenced on an Illumina NovaSeq 6000 instrument at Zymo Research.

Preparation of RRBS libraries

500 ng of starting input genomic DNA was digested with 30 units of MspI (NEB). Fragments were ligated to pre-annealed adapters containing 5′-methyl-cytosine instead of cytosine according to Illumina's specified guidelines. Adaptor-ligated fragments $\geq$50 bp in size were recovered using the Zymo DNA Clean & Concentrator-5. The fragments were then bisulfite-treated using the Zymo EZ DNA Methylation-Lightning Kit. Preparative-scale PCR was performed and the resulting products were purified with Zymo DNA Clean & Concentrator-5 for sequencing on an Illumina NovaSeq 6000 platform. WGBS libraries were sequenced at Zymo Research.

Processing of Dnmt1-TOP-seq data

Filtering of raw read was performed using cutadapt 4.4.[63] Firstly, only reads containing 5′ adaptors were retained for further analysis and followed by the trimming of 3′ adapter (-e 10 -m 70 -q 0 -O 20 -action-none -discard-untrimmed). The subsequent priming oligonucleotide sequence and an adjacent genomic region were identified and rectified using an in-house perl 5 script (http://www.perl.org/). Finally, reads were filtered by length (-m 15 -q 10). FastQC 0.11.9 was used to assess the overall quality distribution of the data. BWA MEM[64] was employed to align genomic reads to the reference mouse genome. Mapped reads were filtered using samtools (-q 30 -F 0 $\times$ 800 -F 256).[65] Reads were then assigned to a nearest CG target and deduplicated utilizing an in-house R 4.3.0 script (https://www.R-project.org) employing GenomicRanges,[66] data.table (https://github.com/Rdatatable/data.table), ShortRead,[67] dplyr,[68] Rsamtools[69] and gUtils (https://github.com/mskilab-org/gUtils) packages. Dnmt1-TOP-seq signal for each genomic element was calculated as a fraction of identified (coverage $\geq$1) CpG targets within the region of interest.

Processing of WGBS and RRBS data

Raw reads underwent adapter and quality trimming using Trimgalore 0.6.4 (https://github.com/FelixKrueger/TrimGalore). FastQC 0.11.9 was used to assess data quality control. Non-directional alignment to the reference mouse genome was conducted with Bismark 0.22.3.[70] Methylated and unmethylated read totals for each CpG site were called using MethylDackel 0.5.0 (https://github.com/dpryan79/MethylDackel) using standard parameters. Unless stated otherwise, only CpGs with a minimum of 5 read coverage were used for the analysis. Methylation levels for each genomic element were determined as the average methylation of all CpGs within that element.

Reference genome annotation

Mouse (*Mus musculus*) reference genome (GRCm38) sequence in fasta format was downloaded from GENCODE database.[76] Reference coding transcripts were retrieved from the NCBI database (https://ncbi.nlm.nih.gov/). RepeatMasker annotated repeats were obtained from the UCSC FTP. CGI, CGI shelves and shores were retrieved using the annotatr R package.[71] Coding and non-coding gene promoters were downloaded from the EPD database.[77] Coding protein and pseudogenes (processed and unprocessed) were extracted from the GENCODE genome annotation. Silencers were downloaded from silencersDB (http://health.tsinghua.edu.cn/SilencerDB). Enhancers were downloaded from EnhancersAtlas2,[78] active and poised enhancers marks (ENCFF462XPD, ENCFF188LEW) and CTCF sites (ENCFF832AQF) were downloaded from the ENCODE project (https://www.encodeproject.org/). All other genomic elements were retrieved GENCODE genome annotation (M23).

Functional enrichment analysis

EnrichedHeatmap package[72] was utilized to illustrate methylation, Dnmt1-TOP-seq and ChIP-seq signals across genomic sites. ComplexHeatmap[73] was employed to generate correlation and CGI methylation heatmaps. Biological process GO enrichment analysis of promoter CGI sets was conducted using the clusterProfiler package[74] with *p*-value adjusted by the Benjamini-Hochberg method. Genomic element enrichment was computed by building a contingency table of all identified targets per each element and Fisher's exact test was used to estimate the odds ratio and significance for the enrichment or depletion.

Time-course data clustering

Fuzzy c-means clustering was applied using M-fuzz package[75] to evaluate DNA methylation and DNMT1 specific activity changes during mESC state transition. CGIs were grouped based on the number of detected targets per CGI or average methylation levels and values per each CGI were normalized to a mean of zero and a standard deviation of one. Fuzzier *m* was calculated using *mestimate()*

function from the M-fuzz package. The optimal number of clusters was established by analyzing the minimal distance between cluster centroids and subsequent manual inspection. CGIs from selected clusters were intersected with promoters from EPS database and used for GO enrichment analysis.

Sanger bisulfite sequencing

Sanger sequencing was performed as described previously[32] and CpG methylation status was evaluated using BISMA tool.[79] Primer sequences are listed in Table S3.

RT-qPCR

RT-qPCR was conducted as previously described.[32] Primer sequences (Metabion) are presented in Table S4.

Western blotting

Cells plated in 6-well plates were prewashed with PBS and scraped into 1.5 mL tubes, and then lysed for 30 min on ice in 50 μL RIPA buffer: 50 mM Tris-HCl (pH 7.4), 150 mM NaCl, 1% Triton X-100, 0.1% sodium deoxycholate, 10 mM KF, 1 mM Na_3VO_4, 5 mM EDTA and Halt Protease Inhibitor Cocktail (ThermoFisher Scientific). Supernatants were collected by centrifugation for 20 min at 20 000 × g at 4°C and protein concentration was determined by the BCA assay (ThermoFisher Scientific). 7.5 μg of protein samples were subjected to 10% SDS-PAGE and then transferred to PVDF membrane (Milipore) by semidry blotting. The membranes were blocked with 3% BSA (Roth) solution in PBS-T buffer for 1 h at room temperature. Next, membranes were incubated with anti-DNMT1 (1:1000; ab87654, Abcam), anti-UHRF1 (1:1000; sc-373750, SantaCruz), anti-DNMT3A (1:1000; sc-373905, SantaCruz), anti-DNMT3B (1:1000; PA1-884, Invitrogen) and anti-GAPDH (1:5000; sc32233, SantaCruz) overnight in PBS-T buffer at 4°C. Membrane bound primary DNMT1, and DNMT3B antibodies were detected by horseradish peroxidase-conjugated secondary anti-rabbit IgG antibody (1:10000; 31460, Invitrogen), DNMT3A, UHRF1 and GAPDH - secondary anti-mouse IgG antibody (1:10000; 31430, Invitrogen) by incubation or 1 h at room temperature. At each step, membranes were washed at least three times with PBS-T. Membranes were visualized with ChemiDocTM imaging system using SuperSignal West Pico PLUS Chemiluminescent Substrate (ThermoFisher Scientific).

Statistical analysis

Quantitative RT-PCR and HPLS/MS data points represent mean and standard deviation of three independent biological replicates. Differences between groups were evaluated by *t* test, with statistical significance at $p < 0.05$ using GraphPad Prism 8.0. The statistical tests for bioinformatic analysis were performed using R 4.3.0 and are detailed in the figure legends and method sections.